



Subduction flux modulates the geomagnetic polarity reversal rate

Mark W. Hounslow^{a,*}, Mathew Domeier^b, Andrew J. Biggin^c

^a Lancaster Environment Centre, Univ. Lancaster, Lancaster LA1 4YB, UK

^b Centre for Earth Evolution and Dynamics (CEED), University of Oslo, NO-0316 Oslo, Norway

^c Geomagnetism Lab., Earth and Ocean Sciences, Univ. Liverpool, Liverpool, UK



ARTICLE INFO

Keywords:

Subduction rate
Reversal rate
Geomagnetic polarity
Core-mantle boundary
Detrital zircons
Paleogeographic-models

ABSTRACT

Ascertaining the cause of variations in the frequency of geomagnetic polarity reversals through the Phanerozoic has remained a primary research question straddling paleomagnetism and geodynamics for decades. Numerical models suggest the primary control on geomagnetic reversal rates on 10 to 100 Ma timescales is the changing heat flux across the core-mantle boundary and that this is itself expected to be strongly influenced by variations in the flux of lithosphere subducted into the mantle. A positive relationship between the time-dependent global subduction flux and magnetic reversal rate is expected, with a time delay to transmit the thermal imprint into the lowermost mantle. We perform the first test of this hypothesis using subduction flux estimates and geomagnetic reversal rate data back to the early Paleozoic. Subduction area flux estimates are derived from global, full-plate tectonic models, and are evaluated against independent subduction flux proxies based on the global age distribution of detrital zircons and strontium isotopes. A continuous Phanerozoic reversal rate model is built from pre-existing compilations back to ~320 Ma plus a new reversal rate model in the data-sparse mid-to-early Paleozoic. Cross-correlation of the time-dependent subduction flux and geomagnetic reversal rate series reveals a significant correlation with a time delay of ~120 Ma (with reversals trailing the subduction flux). This time delay represents a value intermediate between the seismologically constrained time expected for a subducted slab to transit from the surface to the core-mantle boundary (~150–300 Ma), and the much shorter lag time predicted by some numerical models of mantle flow (~30–60 Ma). While the reason for this large discrepancy remains unclear, it is encouraging that our novel estimate of lag time represents a compromise between them. Although important uncertainties in our proposed relationship remain, these results cast new light on the dynamic connections between the surface and deep Earth, and will help to constrain new models linking mantle convection, the thermal evolution of the lowermost mantle and the geodynamo.

1. Introduction

Earth contains two great heat engines that meet at the core-mantle boundary (CMB) and interact thermally across it. Vigorous convection occurs in both the core and mantle, but operates on vastly different timescales, with flows in the core seven orders of magnitude faster than those in the lower mantle (Biggin et al., 2012). Together with the much higher thermal diffusivity of the metallic core, that vigorous convection ensures that lateral temperature variations in the uppermost core are much lower (< 1 K) than those in the overlying lowermost mantle (several hundreds of Kelvin or more).

This implies that the mantle enforces heat flux constraints on the core, dictating how fast the core cools, and controlling its vigor and style of convection. Core convection is necessary to sustain the geodynamo against Ohmic losses (energy dissipated by electrical resistance) and therefore it seems entirely plausible that changes in the

thermal structure of the mantle, resulting from its slow convection, will influence the behaviour of the geomagnetic field on timescales of tens to hundreds of millions of years (Buffett, 2015). Variations in CMB heat flow of tens of percent of the total are predicted for the last few hundred million years (Biggin et al., 2012; Buffett, 2015). The fact that the geomagnetic field also exhibits its strongest variations on such timescales (Constable and Johnson, 2005) re-enforces the idea that mantle-induced changes in CMB heat flow should be detectable in paleomagnetic records.

The best-defined paleomagnetic record for documenting such long-time variations is geomagnetic polarity, which shows that the average duration of single polarity chrons varies from ca. 30 ka to > 10 Ma (Ogg, 2012). Although individual chron length exhibits a stochastic pattern, there is a strong nonstationary in the average reversal frequency measured over a few million years or longer (McFadden and Merrill, 1997; Constable, 2000). The precise nature of this long

* Corresponding author.

E-mail addresses: M.hounslow@lancs.ac.uk (M.W. Hounslow), mathew.domeier@geo.uio.no (M. Domeier), A.biggin@liv.ac.uk (A.J. Biggin).

timescale variation in the reversal record has been the subject of much debate (Gallet and Hulot, 1997; McFadden and Merrill, 1997; Lowrie and Kent, 2004; Shcherbakov and Fabian, 2012) but the basic pattern in the Phanerozoic of near evenly-spaced superchrons interspersed with intervals of reversals is clear (Gallet and Pavlov, 2016).

Previous studies have speculated upon causal links between variations in reversal frequency and expressions of mantle processes at the surface (e.g. Larson and Olson, 1991; Eide and Torsvik, 1996; Courtillot and Olson, 2007). Most of these have relied on thermal forcing of the geodynamo by mantle convection as the key mechanism. Recently, greater clarity from numerical geodynamo simulations has suggested how this relationship may operate (e.g. Olson and Christensen, 2006; Olson, 2007; Aubert et al., 2009; Driscoll and Olson, 2009; Wicht et al., 2010). Olson and Amit (2014) summarise this as a tendency for the magnetic field to have higher reversal rates when the mantle acts to make CMB heat flow higher or more heterogeneous, particularly when it cools the CMB (and hence increases heat flow) in equatorial or polar regions.

The principal source of buoyancy in the mantle—and hence the primary driver of its convection—is the sinking of cold lithospheric slabs subducted at destructive plate margins (Wada and King, 2015). These slabs may stagnate temporarily in the upper or mid-mantle but ultimately sink through the lower mantle, as evident by the continuation of fast seismic wavespeed anomalies down to the CMB (van der Meer et al., 2010, 2018; Shephard et al., 2017). In numerical models of mantle flow (e.g. Steinberger and Torsvik, 2012), sinking slabs thin the thermal boundary layer at the base of the mantle, increasing CMB heat flow directly below them. The time-dependent, global volumetric flux of lithosphere being subducted at trenches could therefore be related to both the magnitude and heterogeneity of CMB heat flow at some later time.

Geodynamic studies specifically aimed at constraining the lag time between variations in surface heat flow (and hence the subduction flux) and CMB heat flow are rare, but suggest a delay of 30–60 Ma (Biggin et al., 2012; Olson et al., 2013; Zhang and Zhong, 2011), although this is highly dependent on the choice of viscosity and temperature profiles in the models. Seismic tomographic models, by contrast, have been used to argue that it takes sinking lithospheric slabs > 100 Ma to penetrate the mid-lower mantle (~1800 km depth) (van der Meer et al., 2010, 2018; Domeier et al., 2016). Whatever the transit time for a slab (and the thermal anomaly associated with it) to arrive in the lowermost mantle, the response of the geodynamo may be subject to a further lag of several tens of Ma, as stratified layers in the uppermost core change thickness in response to the changing conditions of heat flow across the CMB (Buffett, 2015). Notwithstanding whether the core is (or was) stably stratified, we would expect variations in subduction flux at the surface to modulate the reversal frequency with a lag time of at least several tens of millions of years and probably > 100 Ma. New insights into the sensitivity and temporality of this expected relationship can therefore be attained through comparison of global subduction flux and geomagnetic reversal rate records, but this comparison needs to be performed over a time scale of several hundred million years.

At the outset, it is important to note that there are potentially confounding issues with the hypothesis that geomagnetic behaviour can be linked to preceding changes in the subduction flux. Firstly, geodynamo models that predict sensitivity to global heat flow also predict strong dependence on its geographical distribution (Glatzmaier et al., 1999; Olson et al., 2010). Secondly, the dynamics and material properties of the lowermost mantle are poorly understood and sinking slabs may interact with extant materials in variable and unexpected ways (Hunt et al., 2012; Steinberger and Torsvik, 2012). Third, before the thermal effects of descending slabs even reach the CMB, the shift in mass that they present may well modify Earth's moment of inertia tensor, causing true polar wander to occur (Gold, 1955; Steinberger and Torsvik, 2010). This could rotate the entire CMB heat flux pattern in the reference frame of the geodynamo, potentially also causing changes in

geomagnetic reversal rate but with a much shorter time lag (Biggin et al., 2012). Finally, the dynamics of the lowermost mantle, namely the generation of mantle plumes, may play an active role in shaping ensuing plate tectonics at the surface (Dziewonski et al., 2010). Because the departure of mantle plumes can also modify the CMB heat flux, and thus the geodynamo (Biggin et al., 2012); changes to the geomagnetic field could also predate surface tectonic developments, as well as follow from them. However, before any of these possible complexities can be addressed, it must first be determined if any correlation between surface tectonics and geomagnetic field behaviour can be discerned. To this end, we here provide the first statistical comparison of global subduction flux and geomagnetic reversal rates extending back to the early Paleozoic.

2. Subduction flux

At a global scale, subduction flux is the time-dependent volume of lithosphere that is subducted along convergent margins. The calculation of the subduction flux therefore requires knowing both convergence rates and the thickness of oceanic lithosphere, globally, for the duration of the interval of interest. Unfortunately, owing to the loss of oceanic lithosphere to subduction, paleogeographic models that attempt to reconstruct the tectonic plates and their kinematics become progressively uncertain backwards in time (Torsvik et al., 2010). The geographical distribution of oceanic lithospheric thickness is particularly poorly known in the past, and there are no publically-released global reconstructions of oceanic lithospheric thickness or age (from which lithospheric thickness can be estimated) prior to the Mesozoic. However, recently developed full-plate tectonic models allow computation of global convergence rates back into the Paleozoic. These models include globally-networked plate boundaries, a full-accounting of crustal and oceanic lithospheres, and a time-continuous kinematic evolution (Domeier and Torsvik, 2018). We therefore opt to use the subduction area flux (SAF; the global surface area of lithosphere subducted over an arbitrary unit time), which can be calculated from global convergence rates alone, as a proxy for the true (volumetric) subduction flux.

Estimates of the SAF can be derived from a full-plate tectonic model by either direct computation of the total subducted area per unit time, or by determination of the seafloor production (spreading) rate (SPR) that must offset the SAF because the surface area of the Earth is constant (and assuming plate deformation to be negligible at the global scale). Although there are a number of Mesozoic-Cenozoic plate models available, at present there exists only two alternative full-plate models that extend continuously from present day back into the Paleozoic: a 0–600 Ma model developed at the University of Lausanne (Stampfli and Borel, 2002; Stampfli et al., 2013; Vérard et al., 2015; hereafter “V15”) and the 0–410 Ma model of Matthews et al. (2016) (hereafter “M16”), which is based on the 0–230 Ma model of Müller et al. (2016) and the 250–410 Ma model of Domeier and Torsvik (2014). The model of Müller et al. (2016), in turn, is based on the earlier 0–200 Ma full-plate model of Seton et al. (2012). While the latter models are all publically-distributed, the Lausanne model is now industry-owned, and is therefore difficult to scrutinize.

Fig. 1a shows a comparison of both SAF curves derived from the V15 and M16 plate models, generated by direct computation of the subducted area through time. The V15 SAF curve was calculated and presented by Vérard et al. (2015), whereas the M16 SAF curve was computed in this study (extracted from the M16 plate model) by methods described in the Supplementary information. Alternative approaches to computing the SAF to exclude contributions from model artefacts and non-subducting convergent boundaries (i.e. transpressive boundaries) are also discussed in the Supplementary information (Supplementary Fig. S1). Also shown in Fig. 1a is a Mesozoic-Cenozoic SPR curve (Coltice et al., 2013) based on the plate model of Seton et al. (2012). Because M16 is partly an update of Seton et al. (2012), the SPR

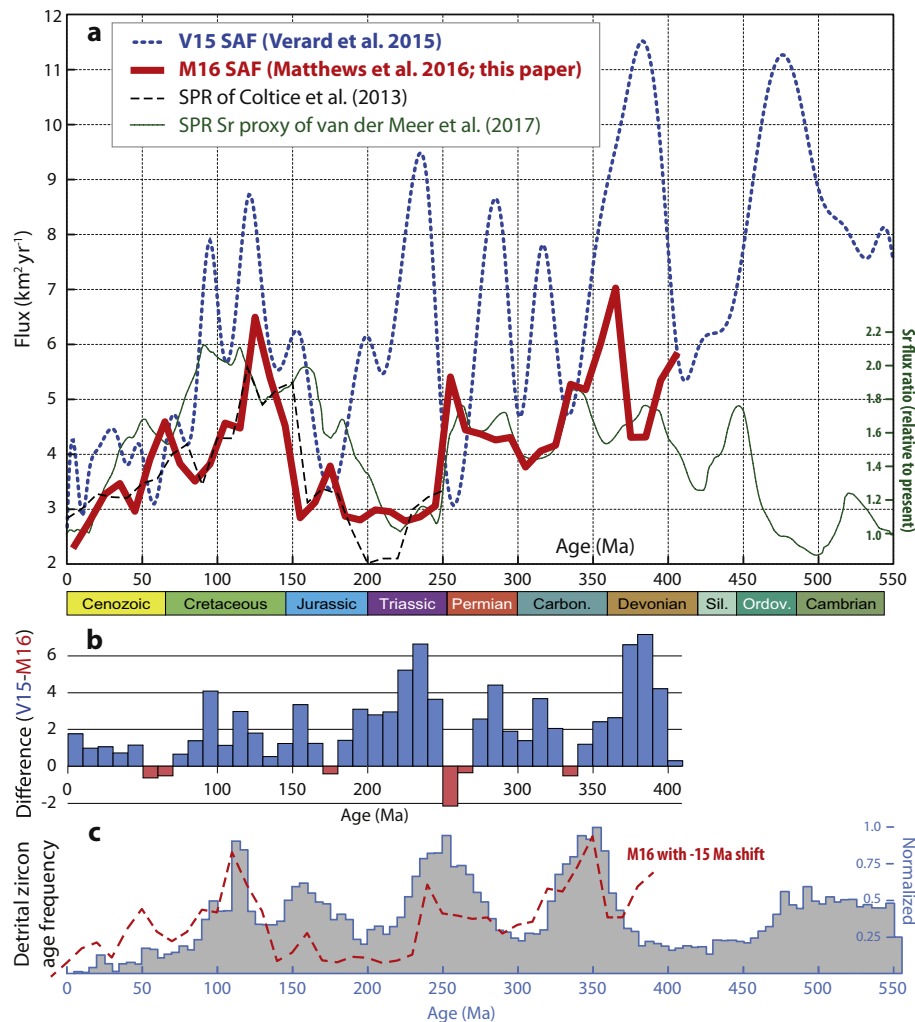


Fig. 1. a) Subduction area flux (SAF) and seafloor production (SPR) rates from previous studies and this work. The V15 SAF was calculated by [Vérard et al. \(2015\)](#), based on the University of Lausanne geodynamic model (now industry owned) that extends back to 600 Ma. The M16 SAF is calculated in this paper, based on the model of [Matthews et al. \(2016\)](#) which extends to 410 Ma (see Supplementary materials). The SPR of [Coltice et al. \(2013\)](#) is derived from the plate model of [Seton et al. \(2012\)](#), extending back to the Early Triassic (250 Ma). The SPR Sr proxy is based on the estimated ‘mantle’ strontium flux calculated by [van der Meer et al. \(2017\)](#) and extends into the Precambrian. b) The time-dependent differences in estimated flux according to the V15 and M16 models; blue (red) bars highlight those intervals where V15 (M16) report higher rates. c) Normalized detrital zircon age frequency based on the database of [Voice et al. \(2011\)](#); see text for details. Red dashed line shows the M16 SAF for comparison, after a 15 Ma shift applied according to the ‘crystallization delay’ detailed in the text. (For interpretation of the references to color in this figure legend, the reader is referred to the web version of this article.)

curve of [Coltice et al. \(2013\)](#) and the 0–250 Ma segment of the M16 SAF curve are not entirely independent, but their similarity underscores the expected equivalence of the time-dependent SAF and SPR.

2.1. Subduction flux since the Jurassic

The M16 SAF (and the SPR of [Coltice et al., 2013](#)) is characterized by relatively low, modern-day-like rates ($\sim 2\text{--}4\text{ km}^2\text{yr}^{-1}$) in the Triassic to mid-Late Jurassic (250–150 Ma), high rates ($> 4\text{ km}^2\text{yr}^{-1}$) in the latest Jurassic and Early Cretaceous (150–100 Ma), and a general decline from high rates to modern-day rates through the Late Cretaceous and Cenozoic (100–0 Ma) ([Fig. 1a](#)). The V15 SAF curve exhibits a similar trend between 180 and 0 Ma, showing a moderate SAF in the Early-Middle Jurassic (180–160 Ma) and Late Cretaceous to Cenozoic (80–0 Ma) separated by high rates in the Late Jurassic and Cretaceous (160–80 Ma). However, the numeric values of the SAF estimated by V15 are significantly higher than those of M16 for most of the last 180 Ma, most notably during the Late Jurassic to mid-Cretaceous (160–90 Ma) ([Fig. 1b](#)).

Alternatively, [Rowley \(2002\)](#) and [Cogné and Humler \(2004\)](#) have suggested that the SPR (and thus the SAF) of the last 180 Ma has been effectively constant. However, neither of those analyses is based on full-plate tectonic reconstructions. The argument of [Rowley \(2002\)](#) is based on the modern-day area versus age relationship of preserved oceanic crust and the assumption that the oceanic crust consumed at subduction zones has a uniform age distribution. This assumption has not been validated, and the modern-day area versus age relationship of oceanic

crust can be equally well explained by a temporally variable SPR ([Coltice et al., 2013](#)). With a different approach, [Cogné and Humler \(2004\)](#) tried to directly calculate the time-dependent SPR for the last 180 Ma from the surface area between preserved isochrons. They calculated global rates by extrapolating across vast regions of lost (subducted) oceanic lithosphere, without reference to a detailed paleogeographic model. For these reasons we dismiss the relatively flat SPR estimates of [Rowley \(2002\)](#) and [Cogné and Humler \(2004\)](#).

[van der Meer et al. \(2014\)](#) also presented an estimate for the SAF from 0 to 250 Ma, based on a proposed paleogeographic proxy: the time-dependent global length of subduction zones (GLSZ). Using both plate reconstructions and seismic tomography (to identify subducted lithosphere in the mantle), their time-dependent estimate of the GLSZ (and by their argumentation, the SAF) is approximately unimodal with a peak in the Late Jurassic–Early Cretaceous (~ 150 Ma), consistent to first-order with the trend of the V15 and M16 SAF curves ([Supplementary Fig. S3](#)). However, we contend that GLSZ estimates provide a poor proxy for the SAF because globally averaged convergence rates are not constant through time. This means that the GLSZ will under- or over-represent the SAF for times when the globally averaged convergence rate is not identical to that of the present-day, or whatever constant rate is assumed ([Supplementary Figs. S2 and S3](#)).

2.2. Subduction flux in pre-Jurassic time

For pre-Jurassic time, when full-plate reconstructions (from which the SAF estimates are derived) are built with entirely synthetic oceanic

lithosphere, the V15 and M16 SAF estimates are very different (Fig. 1a). Starting at 410 Ma, the M16 curve shows relatively high rates in the Devonian to Early Carboniferous (410–325 Ma), moderate rates ($\sim 4 \text{ km}^2 \text{ yr}^{-1}$) in the Late Carboniferous and Permian (325–250 Ma), and a sharp decrease at ~ 250 Ma following a brief increase in the latest Permian. 250 Ma coincides with the end of the 410–250 Ma plate model of Domeier and Torsvik (2014) that underlies M16, so the sharp change in the SAF at this time may partly be an artefact of this model-changeover; a correspondingly sharp change at this time is observed in the GLSZ extracted from M16 (Supplementary Fig. S2). However, as will be shown later, an independent SAF proxy otherwise provides support for this Permo-Triassic inflection (green curve in Fig. 1a). Throughout the late Paleozoic, the numeric estimation of the M16 SAF remains between ~ 3.5 and $7 \text{ km}^2 \text{ yr}^{-1}$, slightly higher than the Mesozoic-Cenozoic average, but generally within the same range. In contrast to the M16 estimates, the V15 SAF curve exhibits oscillations of much higher frequency and greater amplitude between 410 and 250 Ma, spanning rates of ~ 3 to $11.5 \text{ km}^2 \text{ yr}^{-1}$. A similarly-timed relative high is observed in both V15 and M16 in the Late Devonian (380–360 Ma), but their trends are otherwise dissimilar for the remainder of the late Paleozoic and V15 exhibits a sharp increase in rate at ~ 250 Ma when M16 shows a rapid decrease. The V15 SAF estimate also remains very high during the Triassic (250–200 Ma) when M16 exhibits exclusively low rates. The V15 SAF curve extends backward from 410 Ma to the beginning of the Paleozoic, showing an Early Ordovician peak in flux (~ 475 Ma), but no comparison can be made with M16 as the model of Domeier and Torsvik (2014) extends only to 410 Ma.

Because the V15 plate model is now proprietary, it cannot be interrogated and the reason for the pronounced differences between the V15 and M16 SAF curves cannot be determined here. A qualitative examination of the Triassic reconstructions presented by Stampfli et al. (2013) suggests that some of the differences likely relate to more complex intra-Panthalassa subduction in the V15 plate model, although there are undoubtedly other factors involved. Nevertheless, the rapid and large amplitude swings in the V15 SAF present a good opportunity for evaluation against alternative, observation-based subduction flux proxies, as presented below. Those subduction flux proxies also present the opportunity to assess the early Paleozoic segment of the V15 SAF curve, for which M16 can offer no comparison.

2.3. Independent subduction flux proxies

To evaluate the V15 and M16 SAF estimates, we consider potential subduction flux proxies that are independent of the plate models. The global subduction flux is the summation of changes occurring locally along subduction zones, so a reasonable place to begin looking for a proxy of the subduction flux is along active margins. Active margins are associated with a variety of geological processes related to crustal growth and destruction, notably growth includes the construction of accretionary complexes, the emplacement of ophiolites and the generation of magmatic arcs. The time and geographical distribution of these different assemblages, could then be expected to reflect changes in the subduction flux. However, a closer look reveals the use of ophiolites and accretionary complexes to be unsuitable.

Ophiolite emplacement, although now recognized to occur in a variety of geodynamic settings, is a highly-discontinuous process that is generally associated with subduction initiation or major plate reorganization (Agard et al., 2007; Dilek and Furnes, 2011), and so is not suitable as a proxy of progressive (continuous) changes to global subduction. The construction of accretionary complexes is likewise complicated by the competing effects of subduction erosion, and the fact that the exhumation of high-pressure/low-temperature blueschists (as a marker of accretionary prism construction) is also a discontinuous phenomenon (Agard et al., 2009). It is nevertheless interesting to note that the temporal distribution of both ophiolite and blueschist occurrences appear to share a peak in the Late Jurassic to Cretaceous

(Supplementary Fig. S4), similar to that observed in the SAF curves of Fig. 1a, suggesting that even with their discontinuous formation/low preservation potential, the occurrence of ophiolites and blueschists may crudely reflect trends in global subduction.

2.3.1. The detrital zircon proxy

In contrast to ophiolite emplacement and blueschist exhumation, the generation and evolution of magmatic arcs can more continuously (on geologic timescales) mimic the temporal and spatial changes of subduction zones, and continental magmatic arcs are comparatively less susceptible to being destroyed by later subduction-erosion processes. Furthermore, because larger subducted areas may generate greater volumes of magma (Hughes and Mahood, 2008), global fluctuations in arc magmatism may accurately track variations in the global subduction flux. Subduction zone models suggest that faster convergence rates may capture proportionally more of the down-going crustal materials (Roda et al., 2010), which may enhance arc-magma production rates (Hughes and Mahood, 2008). Fluctuations in global arc magmatism, in turn, can be tracked through dating and isotopic studies of detrital zircons (Voice et al., 2011; Barth et al., 2013; Roberts and Spencer, 2015). Age-frequency distributions of detrital zircons from arc-related terranes therefore potentially provide an independent proxy for temporal fluctuations in the global subduction flux (Condie et al., 2017). The dominant age populations of detrital zircons in arc terranes are generally close to the age of host sediment formation (Cawood et al., 2012), indicating little age-bias from long-term ‘storage’ in upper crustal level intrusions. However, a time-lag or ‘crystallization delay’ is expected between the time-dependent subduction flux (as measured at the trench in tectonic models) and the crystallization of arc-magmas (as reflected by zircon ages) that are derived from processes initiated by partial melting of the mantle wedge above the subducting lithosphere.

There are, however, caveats with this relation of detrital zircon age distributions to global arc magmatic activity and ultimately the subduction flux, namely the assumptions that: (1) the detrital zircon record provides a globally uniform temporal and spatial sampling of the true arc magmatic record, (2) that zircon ages have not been widely reset by high-grade metamorphism or crustal re-melting, (3) that zircons generated by other igneous processes (e.g. rifting, intracontinental magmatism) are nominal, and (4) that arc magmatic volumes are relatable to the rate of subduction, rather than being dominated by other parameters (like slab dip or lithosphere age).

To explore the use of detrital zircon age distributions as a proxy for the subduction flux, we used the extensive detrital zircon database of Voice et al. (2011). Pre-processing of the dataset included: (1) extraction of all detrital zircon age data from units with depositional ages < 550 Ma from arc-related settings (forearc, retroarc and backarc), (2) exclusion of zircon ages younger than the host's depositional age minus 5 Ma (i.e. allowing for a 5 Ma uncertainty on the depositional age), (3) exclusion of imprecise zircon ages with 1σ age errors > 50 Ma, and/or $> 20\%$ of the best-estimate of the zircon age. Due to an excessive abundance of zircon dates from North and Central America, we applied a weighting factor of 0.25 to these data (equivalent to summed zircon frequencies of around 3000 in Supplementary Fig. S5), compared to unit weight (1.0) for all other data, to try and minimize regional biases in the age-frequency data. This scaling primarily lessened the magnitude of the zircon age peak at ~ 150 Ma, since this is principally derived from the North and Central American zircon data (Supplementary Fig. S5); there is still some bias after this correction in the study site age distribution. There is also a paucity of detrital zircon ages older than 350 Ma from units in arc settings, but it is not yet clear if this is a true reflection of low rates of arc magma production, or an artefact of preservation.

The resulting detrital zircon age distribution (Fig. 1c) shows broad peaks in the Cambro-Ordovician (475–540 Ma), the Early Carboniferous (330–360 Ma), the mid-Permian to mid-Triassic (230–270 Ma), the Late Jurassic (140–170 Ma), and the late Early Cretaceous

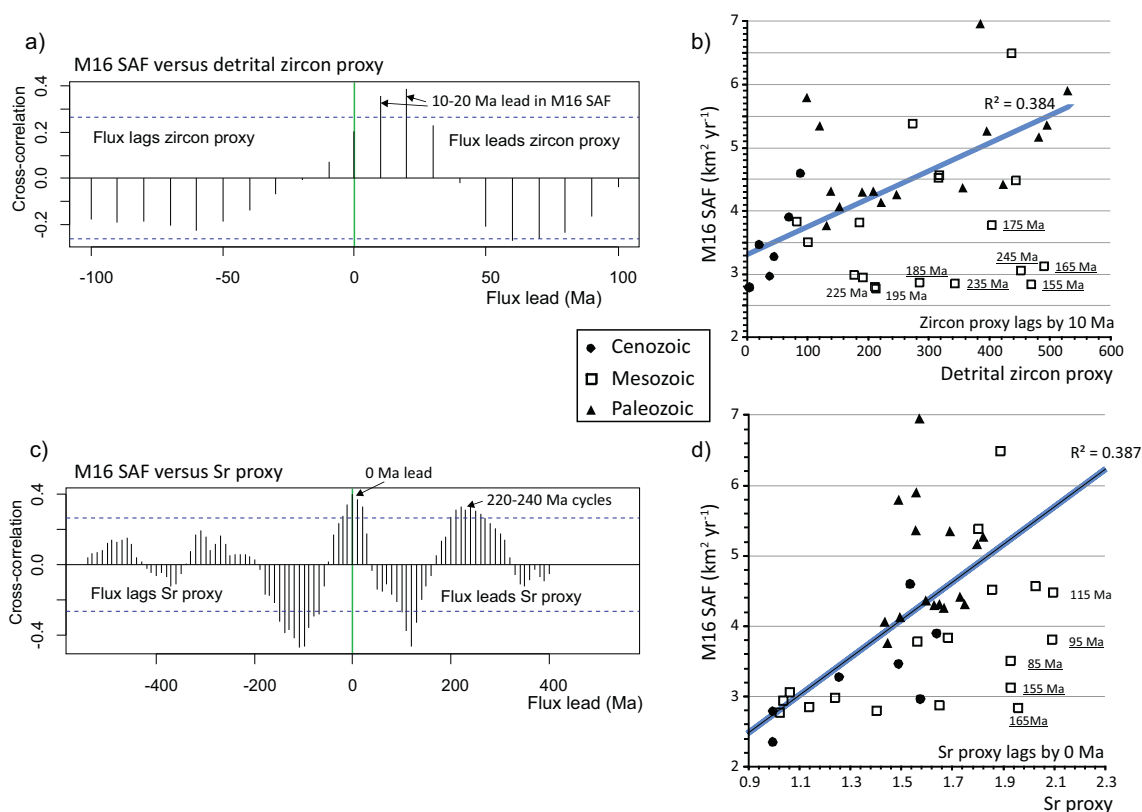


Fig. 2. a) Cross-correlation between the M16 SAF and the detrital zircon proxy, illustrating a ~ 10 – 20 Ma lag ('crystallization delay') in the zircon data. b) Instantaneous comparisons between the M16 SAF and the detrital zircon proxy (with a 10 Ma lag); selected Mesozoic outlier points are labelled with their associated SAF age. The blue line is a linear regression of the data, excluding the six most extreme outliers (underlined). c) Cross-correlation between the M16 SAF and the Sr proxy, showing a peak with a time lag of 0 Ma. d) Instantaneous comparisons between the M16 SAF and the Sr proxy, with selected Mesozoic outliers indicated. The blue line is a linear regression of the data, excluding the four most extreme outliers (age indicated and underlined). Cross-correlations used time series analysis in R (Cowpertwait and Metcalfe, 2009). (For interpretation of the references to color in this figure legend, the reader is referred to the web version of this article.)

(~ 110 Ma). The latter four peaks align well with the intervals of elevated flux observed in the M16 SAF, assuming a slight time delay (~ 15 Ma), as demonstrated by lagged cross-correlation analysis (Figs. 1c, 2a). The ~ 15 Ma delay (zircon ages trailing the SAF) is interpreted as the 'crystallization delay', representing the time interval between a slab entering the trench and zircons crystallizing from arc magmas near the surface. Notably, despite the good fit between these time-series, their comparison at specific times does not always coincide with the 'time-averaged' trend (Fig. 2b). In contrast to the good agreement between the M16 SAF and the detrital zircon proxy, the latter does not resemble the V15 SAF prior to ~ 150 Ma, and the higher-frequency changes observed in V15 are not apparent in the detrital zircon age distribution. This qualitative assessment is confirmed by lagged cross-correlation analysis of these series, wherein no significant positively lagged correlation is detected. These results tentatively suggest that the M16 SAF is more reliable than the V15 SAF over the late Paleozoic-Mesozoic interval.

2.3.2. Mantle Sr isotope proxy

As an alternative to seeking a proxy for the volume of lithosphere subducted along trenches, a proxy for the seafloor production rate can also be used to evaluate the V15 and M16 SAF curves. Because the dominant driver of global sea-level on million year timescales is the changing volume of mid-ocean ridges (Conrad, 2013), existing Phanerozoic eustatic curves (Miller et al., 2005; Haq and Schutter, 2008) could conceivably be inverted to estimate the time-dependent SPR (Gaffin, 1987; Mills et al., 2017). However, because many other factors contribute to sea-level fluctuations, particularly on local to regional scales (Conrad, 2013), it is not generally straightforward to isolate true

'eustatic' changes (Moucha et al., 2008; Spasojevic and Gurnis, 2012), and so the estimation of ancient SPR is unlikely to be reliable by this approach. Alternatively, Jones et al. (1994) and van der Meer et al. (2017) have proposed that strontium isotope data can be used to infer past SPR, because the $^{87}\text{Sr}/^{86}\text{Sr}$ ratio of seawater is sensitive to the flux of strontium from the mantle, which is partly governed by the SPR. The $^{87}\text{Sr}/^{86}\text{Sr}$ ratio of seawater results from the balance of 'continental' input (with high $^{87}\text{Sr}/^{86}\text{Sr}$ ratios) via rivers carrying continental detritus, and 'mantle' input (with low $^{87}\text{Sr}/^{86}\text{Sr}$ ratios) via hydrothermal circulation at mid-ocean ridges and the weathering of island arc and ocean island basalts (Goddéris and François, 1995; Allègre et al., 2010). By quantifying and removing the 'continental' contribution, van der Meer et al. (2017) produced a Sr 'mantle component' flux back to the early Neoproterozoic which they contend tracks the global time-dependent SPR. A notable caveat of this result is that it also reflects the 'mantle' Sr flux from plume-related volcanism (Allègre et al., 2010; Mills et al., 2014).

In Fig. 1a the Sr 'mantle component' curve of van der Meer et al. (2017) (hereafter called the 'Sr proxy') is compared with the V15 and M16 SAF curves. Although the vertical scaling is relative, the trends of the Sr proxy back to 400 Ma show a close correspondence to the M16 SAF curve. In particular, a pronounced low in the Triassic (250–210 Ma) is seen in both series, following an abrupt decline from moderate to high rates in the early to mid Permian (290–260 Ma). This assessment is confirmed by a strong, positive cross-correlation of the two series at a lag time of 0 Ma (Fig. 2c). Outliers among instantaneous comparisons of the series (Fig. 2d), for example in the mid-Cretaceous (115–85 Ma) and Late Jurassic (165–155 Ma), could be related to periods of elevated island arc or plume-related basalt production (Mills

et al., 2014). A second positive cross-correlation of the M16 SAF and Sr proxy is observed at a lag time of 240–220 Ma (Fig. 2c), and reflects a long-term cyclicity common to both series (see also Section 4.2); this long-term cyclicity of the Sr proxy was also recognized by van der Meer et al. (2017).

Unlike the M16 SAF, the V15 SAF curve does not clearly resemble the Sr proxy prior to the Jurassic. In particular, the V15 SAF curve shows a pronounced but brief low in the late Permian followed by high to moderate rates through the remainder of the Triassic, in contrast to the low rates showed by the M16 SAF and Sr proxy (Fig. 1a). In the earlier Paleozoic, before 400 Ma, the Sr proxy suggests that the SPR generally declined back to 500 Ma in the Cambrian, whereas the V15 SAF shows consistently high rates. According to cross-correlation analysis, the V15 SAF curve is not significantly correlated to the Sr proxy for any time lag up to 300 Ma. From these results we again conclude that the SAF curve of M16 is likely more reliable for the late Paleozoic to Mesozoic interval.

3. Geomagnetic reversal rates

The calculation of geomagnetic reversal rates through time requires first knowing the time-dependent geomagnetic polarity history across the time interval of interest, but the geomagnetic polarity timescale is not yet established for the entire Phanerozoic. To determine reversal rates back into the early Paleozoic, we therefore first constructed a new geomagnetic polarity timescale for the last 500 Ma, using a variety of sources described in Table 1.

3.1. Geomagnetic polarity through time

The existing geomagnetic polarity timescale (GPTS) is well validated back to the Late Jurassic, largely from sea floor anomaly data, and the astronomical calibration of the Cenozoic magnetochrons (Ogg,

2012). The mid-Jurassic (M29 to M42) polarity record is taken from Ogg (2012) based on magnetic anomalies in the Japanese western Pacific, which are corroborated by Hawaiian magnetic lineations, that extend back to chron M42 (Tominaga et al., 2015), corresponding to the late Bajocian (~169 Ma). However from around seafloor anomaly M26 back to M42, the relationship to Jurassic stages and polarity data from land-based sections is not currently clear, although land-based records are similar in some parts to the deep tow seafloor anomalies (Gipe, 2013). We follow Ogg (2012) and join the magnetic anomaly and land-based data in the Aalenian (early Middle Jurassic, ~170.7 Ma, chron M45r), in order to allow the polarity timescale to be continued further backward in time.

The magnetic polarity record from the latest latest Carboniferous to Early Jurassic (~300–180 Ma) is largely complete except for two brief gaps in the mid-Sinemurian (early Jurassic, ~195 Ma; Ogg, 2012) and mid-Carnian (late Triassic, ~230 Ma; Table 1); these are gaps of approximately 3 Ma and 1.4 Ma, respectively. However, polarity data between the earliest Middle Triassic and early Carnian (247–235 Ma), proposed by Hounslow and Muttoni (2010), has not been calibrated against constraining radiometric dates, so we construct an age model for this time interval using the methods applied by Hounslow (2016) and Hounslow and Balabanov (2016). The methods and data used are described in the Supplementary data, along with the details of how this new segment has been joined with the Early Triassic polarity data of Li et al. (2016). The Kiaman reverse superchron starts at around 318.8 Ma in the mid Carboniferous and continues into the mid-Permian (Opdyke et al., 2014; Hounslow, 2016). Modern magnetostratigraphic data from the late Carboniferous (180–300 Ma) are sparse, but existing compilations (Molostovsky et al., 2007; Idnurm et al., 1996) suggest reversal frequencies that may have been similar to those of the early Permian.

Prior to the onset of the Kiaman superchron at around 318.8 Ma, the geomagnetic polarity is generally poorly known. Between the mid Carboniferous and the Late Ordovician (320–450 Ma), only two

Table 1

Source data and methods used to construct the geomagnetic polarity timescale through the Phanerozoic (see also SI Tables S1 to S4).

1. Polarity timescale age range	2. Polarity timescale data source	3. Data type	4. Age model construction methods
Brunhes to mid Jurassic (Aalenian)	Ogg (2012), For late Aalenian-Oxfordian using deep tow sea-floor data displayed in his Fig. 26.9 in Gradstein et al. (2012).	Sea floor anomaly composite.	Based on spreading rates with Neogene and younger parts adjusted by cyclostratigraphy
Mid Jurassic (Aalenian) to early Jurassic (mid Sinemurian)	Timescale Creator v7. Based on data in Gradstein et al. (2012).	Land-based sections	Chrons anchored to biostratigraphy. Age model is a spline, adjusted by cyclostratigraphy and Pacific spreading-rate model tied to land-based sections in the late Jurassic (Ogg, 2012).
Early Jurassic (mid Sinemurian) to late Triassic (late Carnian)	Kent et al. (2017)	Newark Basin sections and cores, USA	Cyclostratigraphic, anchored to 201.520 ± 0.034 Ma for the Palisade Sill.
Late Triassic (late Carnian) to base of mid Triassic (early Anisian)	Constructed here using data in Hounslow and Muttoni (2010)	Land-based sections	Pseudo-height manual section-composites (Figs. 3, 5, 6 in Hounslow and Muttoni, 2010) scaled using BChron (SI Fig. s6)
Early Triassic (Induan to late Olenekian)	Li et al. (2016)	Chinese and German land-based sections	Cyclostratigraphic, anchored to Permian age model (SI Fig. s8) and LT1n from Hounslow and Balabanov (2016)
Permian	Hounslow and Balabanov (2016)	Land-based sections	Statistical composite scaled using BChron
Carboniferous (late Viséan- early Serpukovian)	Sources and details in Hounslow (2016)	Canadian land-based sections	Statistical composite scaled using BChron
Late Devonian (mid Frasnian- mid Fammenian)	Constructed here using Supplementary data of Hansma et al. (2015) and Windjana Valley section (SI Fig. S5)	Canning Basin sections, Australia	Statistical composite scaled using BChron (SI Figs. s7, s9, s10)
Mid Cambrian to late Ordovician (Series 3 to early Sandbian)	Sources and details from Hounslow (2016)	Various Land-based sections	Statistical composite scaled using BChron

segments of reasonably well validated polarity data are established: for the late Viséan-early Serpukovian (333 to 327 Ma; [Opdyke et al., 2014](#)), and the mid-Frasnian to late Famennian (376–365 Ma; [Hansma et al., 2015](#)). The geomagnetic polarity data through the late Viséan-early Serpukovian have been calibrated against radiometric dates by [Hounslow \(2016\)](#), whereas the Devonian data of [Hansma et al. \(2015\)](#) remain uncalibrated. We therefore generate a new polarity timescale for the mid-Frasnian to late Famennian interval, following the same approach used for the Middle Triassic (detailed in the Supplementary data). The Frasnian ages differs substantially from the 2012 stage timescale ([Becker et al., 2012](#)), due to the new radiometric data from [Lanik et al. \(2016\)](#), which replaces the older date of [Tucker et al. \(1998\)](#).

Between 493 and 454 Ma (late Cambrian-Late Ordovician), data from several sections allows a composite polarity timescale to be constructed ([Hounslow, 2016](#)), spanning a few million years on either side of the Moyero superchron, which has its older and younger boundaries generally well defined ([Pavlov and Gallet, 2005](#)). Early and mid-Cambrian magnetostratigraphic data is available from Siberia but the somewhat poor consistency between studies makes it difficult to construct a polarity timescale ([Gallet et al., 2003](#); [Rodionov, 2016](#)). Similarly, magnetostratigraphic data is available for the late Ediacaran but a composite polarity timescale is not currently viable ([Schmidt and Williams, 2010](#); [Bazhenov et al., 2016](#)). The new geomagnetic polarity model derived here (list of Phanerozoic chrons) resulting from this analysis is described in the Supplementary data.

3.2. Calculation of reversal rates from the GPTS

Various methods for converting the age of magnetochrons into polarity reversal rates have been proposed ([Table 2](#)), which yield alternative estimates, due to differing assumptions. The most widely used approaches have been the determination of reversal frequency and mean reversal rate ([Naidu, 1971](#); [McFadden and Merrill, 1984](#); [Gallet and Hulot, 1997](#)). These approaches require a decision on the width of the time or ordinal window to smooth the stochastic variations in chron durations, to calculate the reversal rate. The wide use of mean reversal rate is clearly motivated by the early recognition that chron durations are similar to Poisson (exponential) or gamma distributions, in which the mean rate is the key distribution parameter ([Cox, 1968](#); [Naidu, 1971](#); [McFadden and Merrill, 1984](#); [Lowrie and Kent, 2004](#)). Geometric mean reversal rates have some advantageous statistical properties ([Table 2](#)), but have only rarely been used ([Didenko, 2011](#)). These methods all rely on the implicit assumption that the reversal rate is stationary over the width of the age or ordinal-range window ([Constable, 2000](#)), and all require an arbitrary decision on what window width to use ([Gallet and Hulot, 1997](#)), which may vary from a few chrons to many tens of Ma ([Naidu, 1971](#); [McFadden and Merrill, 1997](#); [Lowrie and Kent, 2004](#)). The choice of window width strongly controls the amount of smoothing of the reversal rates. [Constable \(2000\)](#) has overcome the stationarity assumption by using Gaussian kernel density estimates with locally adaptive bandwidths to define highly smoothed reversal rates. Similar methods using local likelihood kernel density estimation are implemented in the LOCFIT routines in R ([Loader, 1997](#); [R Development Core Team, 2005](#)), and can be used to estimate reversal rates via a Poisson process ([Loader, 1999](#); Supplementary Fig. S13).

We instead utilise the inherently smooth chron ordinal versus age relationships (Supplementary Figs. S11 and S12) to derive smoothed chron durations from the least squares gradients in these datasets, as exemplified by principles set out in [Reyment \(1976\)](#) and [Gallet and Courtillot \(1995\)](#). Fitting least squares functions in this way makes no assumptions about stationarity in reversal rates ([Table 2](#)). Least squares (LS) reversal rates are then determined from the gradient of the smoothed chron ordinal versus age relationship (at each chron). We make an objective decision on the best smoothing bandwidth by use of

Table 2
Different methods to determine geomagnetic polarity reversal rates. The first three rate determinations implicitly assume the sequence of *n* chrons (or those covered by window *w*) is from a stationary sequence. Supplementary Fig. S13 shows the impact of these differing ways to estimate reversal rate.

Type and name	How
Reversal frequency ^a	The number of chron bases, <i>i</i> , within a time window, <i>w</i> , with <i>i/w</i> giving the reversal frequency. The age window does not normally correspond to chron boundaries, <i>w</i> is fixed and <i>i</i> varies.
Mean reversal rate ^{a,b}	Given the duration, <i>d_i</i> , of <i>n</i> chrons, the mean reversal rate is: $= 1/(\sum_{i=1}^n d_i)/n$. This gives the same value as reversal frequency, if the age window includes the same <i>n</i> chron bases. In this case for each progressive sequence <i>n</i> is fixed and the sum of the respective chron duration varies. A harmonic mean of $(1/d_i)$ gives the same result.
Geometric mean (GM) reversal rate ^c	Given the duration, <i>d_i</i> , of <i>n</i> chrons, the GM reversal rate is: $1/\sqrt[n]{d_1 d_2 d_3 \dots d_n}$ or the equivalent formula to mean reversal rate but taking $\log(d_i)$ for <i>d_i</i> . The arithmetic mean of $\log(1/d_i)$ gives the same result. Like mean reversal rate, <i>n</i> is fixed for the progressive sequence. The GM reversal rate is the best central tendency-value of the reversal rate, since it honours the fact that chron durations have an approximate exponential distribution (Lowrie and Kent, 2004), so $\log(d_i)$ residuals around the GM mean will be closer to normal distribution. The GM reversal rate will be larger than mean reversal rate (10–30% larger at mean reversal rates $> 5 \text{ Ma}^{-1}$), due to a bias to bigger chron durations for the mean reversal rate. At mean reversal rates $< 5 \text{ Ma}^{-1}$ GM means are 10–80% larger (SI Fig. S13).
Least squares (LS) reversal rate ^d	A least squares regression between the chron ordinal number (<i>o_k</i>) and the age, <i>a_k</i> , of the chron bases, yields the least squares gradient, <i>a</i> , giving the LS reversal rate as $1/a$. Like mean and GM reversal rates, <i>n</i> is often fixed for the progressive sequence. For large <i>n</i> , (or <i>d₁</i> = <i>d₂</i> = <i>d₃</i> ... = <i>d_n</i>) the LS reversal rate will approach the mean reversal rate ($\pm 10\%$), but for smaller <i>n</i> or lower mean reversal rate ($< 5 \text{ Ma}^{-1}$), they will diverge by as much as -30 to $+80\%$ from the mean reversal rate.
Kernel density (KD) reversal rate ^e	A chron density function using kernels, applied to each chron boundary. The method finds a density estimate of the number of reversals per Ma, according to a Poisson process. Like other methods the bandwidth (which controls the amount of smoothing) needs to be decided.

^a Cox (1968).

^b Naidu (1971) and [McFadden and Merrill \(1984\)](#).

^c [Didenko \(2011\)](#).

^d [Reyment \(1976\)](#).

^e [Constable \(2000\)](#).

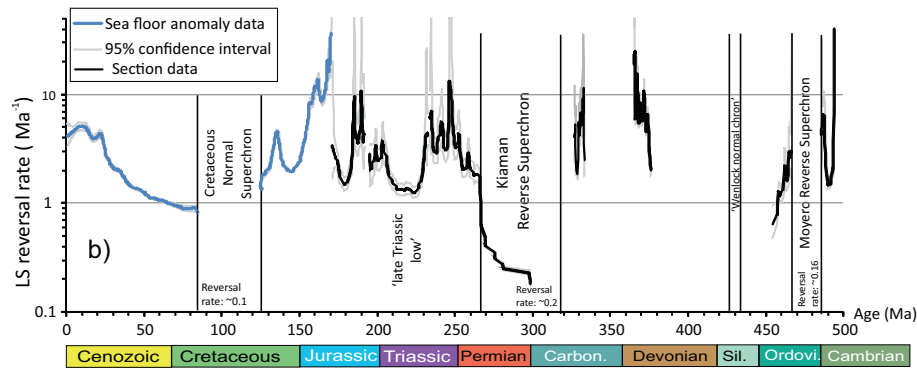


Fig. 3. The LS reversal rate data, derived from the LOCFIT estimating procedure, and the 95% confidence intervals on the LS reversal rates (data reported in Supplementary data). The reversal rate frequency during the superchrons is shown, based on known subchrons within the superchrons.

generalized cross-validation, Akaike information criteria and Mallows Cp, as implemented in the local regression and likelihood methods in the LOCFIT routines in R (Loader, 1997, 1999; James et al., 2013; see Supplementary Table S3). Cross-validation balances the degree of smoothing with the prediction error and model complexity. Local quadratic polynomials were used in local regression procedures. 95% confidence intervals (Loader, 1999) were also estimated for the gradients (chron durations), and converted to confidence intervals on the reversal rates (Fig. 3). A comparison of the various methods to estimate reversal rates for 0–170 Ma is shown in Supplementary Fig. S13.

To convert the LS reversal rates into rates averaged over equal million year increments like the SAF data (at 10 Ma for the M16 model and 5 Ma for V15), we first use the LS reversal rate data at each chron and interpolate into 1 Ma intervals using the local regression function LOESS in R, with a bandwidth of 7.4 Ma (Fig. 4a; Supplementary Table S3). The LOESS extrapolates through the small data gaps in the mid-Sinemurian and mid-Carnian. The final reversal rate estimates at 5 and 10 Ma intervals to match the SAF rates are means of the 1 Ma estimates in each of the 5 Ma or 10 Ma windows, starting from 0 or 5 Ma, respectively. The 1σ uncertainty on the 10 Ma spaced reversal rates is estimated from the standard deviation of the 1 Ma rate values. Large 1σ

largely relate to crossing of superchron boundaries in the age window.

3.3. Paleozoic reversal rate model

To estimate likely reversal rates in the Paleozoic, where robust geomagnetic polarity data is missing for much of the interval between 300 and 450 Ma (Fig. 4a), we define a simple model to fill the gaps. Like many authors, we adopt the assumption that the reversal process differs between single-polarity superchrons and the normal reversing state (Hulot and Gallet, 2003; Lowrie and Kent, 2004), so we estimate the reversal rates in these intervals differently. Specifically, our simple Paleozoic model is defined by the following superchron and superchron-like intervals:

- Kiaman superchron reversal rates are extended to 318.8 Ma (start of the Kiaman Superchron, Hounslow, 2016), using the low rates (0.2 Ma^{-1}) from the Permian–Carboniferous boundary interval.
- The Moyero superchron (466.8–485.6 Ma) is known to have at least one normal chron in the Tremadocian (Yang et al., 2002; Hounslow, 2016), so we use a reversal frequency of 0.16 Ma^{-1} (three reversals over 18.8 Ma).

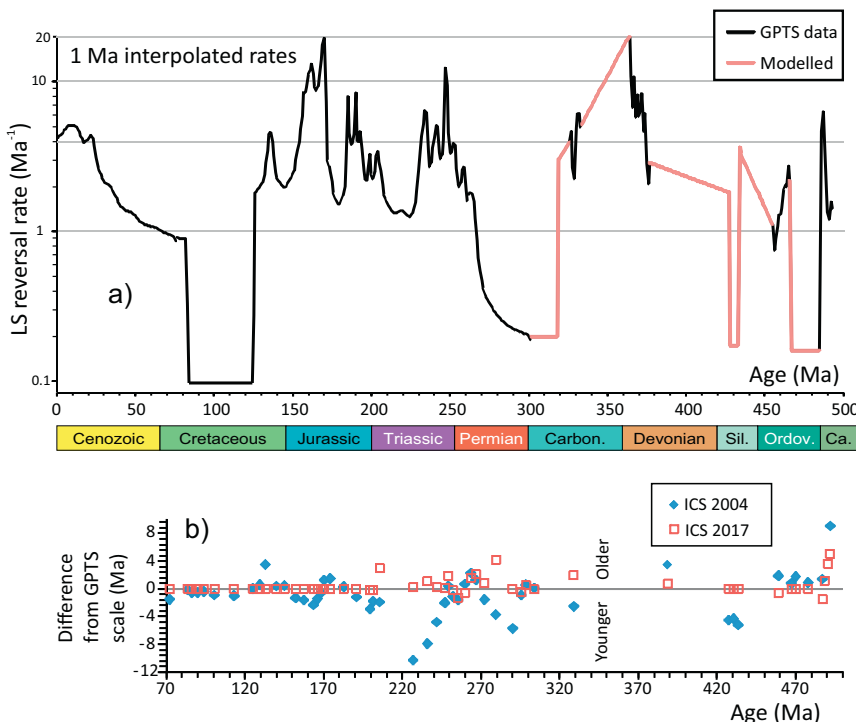


Fig. 4. a) The reversal rates at 1 Ma intervals interpolated from the LS reversal rate at each chron, along with the modelled values of reversal rates in the Paleozoic, where data is absent. b) Time offsets from the geomagnetic polarity time scale (i.e. age of stage bases), as used here, to illustrate the likely scale of age offsets between the SAF data and the geomagnetic polarity. Older (younger) ages indicate SAF ages are older (younger) than the GPTS ages used here. ICS 2004 and 2017 are the stage base ages produced by the International Commission on Stratigraphy, which relate largely (but not entirely) to the timescales in Gradstein et al. (2012, 2004). Prior to 70 Ma, differences are small and $< 0.5 \text{ Ma}$ (not shown).

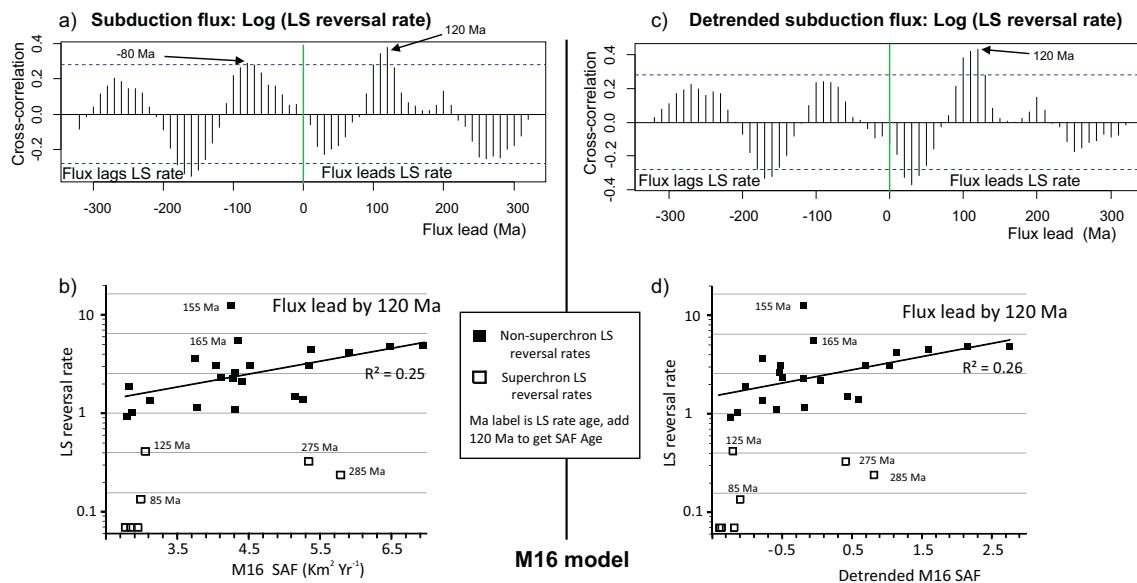


Fig. 5. Cross-correlation between the M16 SAF and the LS reversal rates, using either a) the raw M16 SAF, or c) the de-trended M16 SAF. Both superchRON and non-superchRON data are used in these cross-correlations. Dashed blue lines indicate the 5% significance level (Cowpertwait and Metcalfe, 2009). b) and d) show instantaneous comparisons of these correlations at a 120 Ma SAF lead, with data separated into superchRON and non-superchRON intervals. Selected outlier points are labelled with the age of the LS reversal rate point. The black lines are linear regressions through all the non-superchRON data, indicating a generally positive relationship between the SAF and LS reversal rate. (For interpretation of the references to color in this figure legend, the reader is referred to the web version of this article.)

c) A low reversal rate ('superchRON-like') interval is added in the mid Silurian ('Wenlock chRON', 427.4–433.4 Ma), as suggested by the polarity bias reported by Trench et al. (1993). This 'Wenlock chRON' is assumed to have reversal rates intermediate to the rates of the Kiaman and Moyero superchRONs (i.e. at 0.18 Ma^{-1}), following that there may be some time dependency in the reversal structure (Hounslow, 2016). The remainder of the Silurian (both preceding and postdating this 'Wenlock chRON') are in a usual reversing state of unknown reversal rate (Trench et al., 1993).

At the beginning and end of these superchRONs, we estimate rates extrapolated from those observed to flank other superchRONs. For the start of the Kiaman SuperchRON and 'Wenlock chRON', we assign rates corresponding to the average starting rates for the adjacent Cretaceous Normal and Moyero superchRONs, respectively (i.e. at 2.98 and 3.61 Ma^{-1} respectively; Hounslow, 2016). For the end rate estimate for the 'Wenlock chRON', we assign the mean of the Kiaman and Moyero end rates (at 1.83 Ma^{-1}) from Hounslow (2016). This assumption seems justified by the fact that Paleozoic reversal rates leading into and out of superchRONs show some systematic changes (Hounslow, 2016).

The remaining data gaps in the Paleozoic 1 Ma-interval rate model are filled by linear interpolation between the reversal rates that bound them. This linear interpolation is done in an age versus Log(LS reversal rate) space to reflect the normal-like distribution of the log (reversal rate). The complete Phanerozoic reversal rate model (including both modelled and observation-based rates) is shown in Fig. 4a and uncertainties in Fig. 3.

The timescale of the Paleozoic part of the M16 model is rooted in the global paleomagnetic dataset of Torsvik et al. (2012), which uses the timescale of Gradstein et al. (2004) for age assignments. Although that differs from the new GPTS constructed here, the differences between these timescales are non-systematic and near-invariably below the 10 Ma resolution of the M16 SAF (Fig. 4b), and so they should not significantly impact age-comparisons made between these series. The biggest divergences may be in the Permian and Triassic. Unfortunately, it is not clear what timescale is used in the V15 model, so the potential for artefacts in age-comparisons between the GPTS and V15 SAF

(introduced by timescale differences) cannot be entirely excluded.

Prior to the late Cambrian, reversal frequencies can only be estimated, and may be of the order of $6\text{--}8 \text{ Ma}^{-1}$ (Gallet et al., 2003) during the mid-Cambrian (Series 3) at around 505 Ma (Peng et al., 2012) and decline to ca. 3 Ma^{-1} across the Terrenuvian-Series 2 boundary in the Cambrian at ca. 521 Ma (Kirschvink et al., 1991; Peng et al., 2012). During the late Ediacaran at around 550 Ma, reversal frequency may be as high as 20 Ma^{-1} (Bazhenov et al., 2016). (See Supplementary Information.)

4. Correlations between subduction flux and reversal rates

The statistical relationship between the reversal rates and the subduction flux were examined using conventional time series analysis in R (Cowpertwait and Metcalfe, 2009). We use the Log of the LS reversal rates in this analysis because it is closer to a normal distribution of rates, as seen in the SAF (a similar analysis using linear LS reversal rates is shown in the Supplementary Figs. S14 and S16). We explored the use of the raw SAF data, but also de-trended SAF data, since the average speed of plates appears to generally increase backward in time (Domeier and Torsvik, 2014; Matthews et al., 2016; V  rard et al., 2015). From a statistical perspective, only the M16 SAF has a significant trend in the time series (KPSS trend test, with M16, $p = 0.04$ and V15, $p = 0.1$; Kwiatkowski et al., 1992). The rationale for using the de-trended SAF data is two-fold: 1) the apparent increase in plate speeds backward in time may be an artefact of the growing uncertainty of plate reconstructions rather than a real trend, and 2) it is more appropriate to de-trend the SAF data to compare it against the log LS reversal rates because the latter have no trend in the time series (KPSS trend test, $p = 0.1$; Kwiatkowski et al., 1992).

Cross-correlation of the M16 SAF and reversal rates reveals significant positive correlations at a 80 Ma lag (subduction flux trailing the reversal rate) and a 120 Ma lead (subduction flux leading the reversal rate) (Fig. 5a). Use of the de-trended SAF tends to enhance the importance of the 120 Ma lead of the subduction flux (Fig. 5c). This consistency affirms that the observed correlations are not significantly influenced by or dependent on the long-term, monotonous trend of the

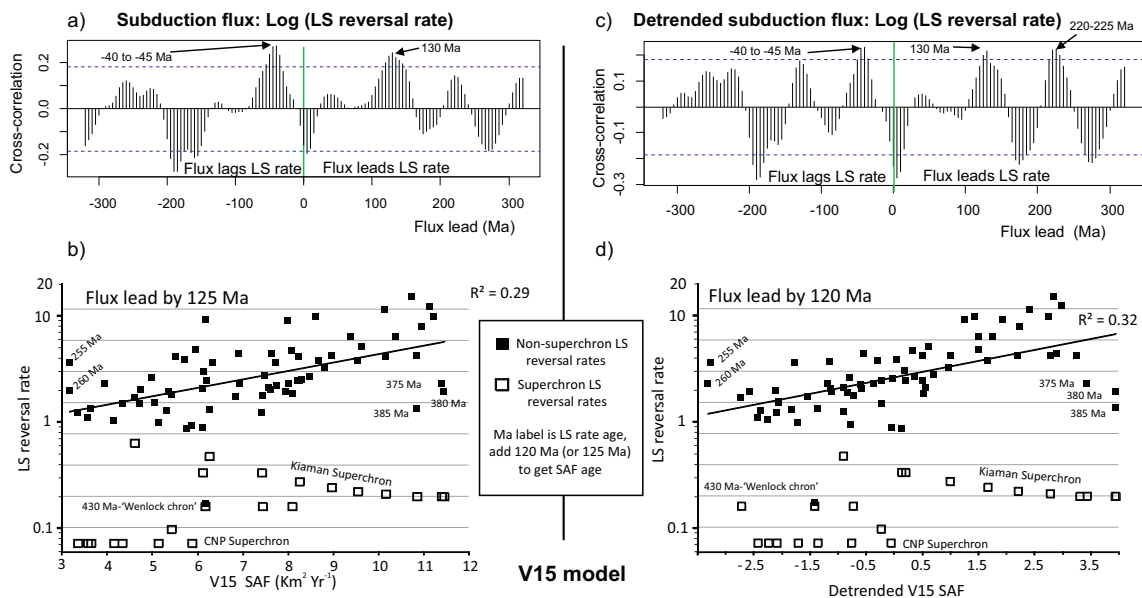


Fig. 6. Cross-correlation between the V15 SAF and the LS reversal rates, using either a) the raw V15 SAF, or c) the de-trended V15 SAF. Both superchρον and non-superchρον data are used in these cross-correlations. Dashed blue lines indicate the 5% significance level (Cowpertwait and Metcalfe, 2009). b) and d) show instantaneous comparisons of these correlations at the specified SAF lead, with data separated into superchρον and non-superchρον intervals. Selected outlier points are labelled with the age of the LS reversal rate point. The black lines are linear regressions through all the non-superchρον data, indicating a generally positive relationship between the SAF and LS reversal rate. (For interpretation of the references to color in this figure legend, the reader is referred to the web version of this article.)

SAF. Similar results are also obtained with cross-correlation of the M16 SAF against linear LS reversal rates (Supplementary Fig. S16). Reversal rates within superchrons are rather poorly defined (in terms of data density) compared to non-superchρον intervals, which have many magnetochrons defining the rates, so the uncertainty in superchρον reversal rates is generally much larger. With this in mind, we unravel the cause of the cross-correlation at a lead at 120 Ma, using superchρον and non-superchρον divisions of data. The correlation is in part controlled by low LS reversal rates in the Cretaceous Normal Superchρον (Fig. 7a), but a positive relationship is also observed outside the temporal frame of the superchrons (Fig. 5b, d), which explains some 25% of the variance. With respect to the 120 Ma leading M16 SAF, the Late Jurassic LS reversal rates (155–165 Ma) seem anomalous, notably corresponding to times that were also observed to be anomalous in the comparisons of the detrital zircon and Sr proxies against the M16 SAF.

For cross-correlations between the V15 SAF and reversal rates, significant positive correlations occur at a 130 Ma lead and a 40–45 Ma lag, for both the raw and de-trended SAF (Fig. 6a, c). The cross-correlation at a lead of 130 Ma is strongly controlled by the LS rate fluctuations in the 140–430 Ma interval and particularly the low rates around the Kiaman superchρον, but it results in the SAF and LS reversal rates being out of phase during the Cretaceous Normal Superchρον (Fig. 7b). Notably, without the high in the V15 SAF during the mid and late Triassic (240–200 Ma), these datasets would show a higher degree of in-phase change. As aforementioned, other subduction flux estimates and proxies are invariably low in the mid- and Late Triassic (Fig. 1), strongly suggesting the high SAF estimated by V15 then to be dubious. The correlations (with an SAF lead) divided into superchρον and non-superchρον comparisons reveals that the non-superchρον LS reversal rates have a consistent relationship with the V15 SAF (explaining some 29–32% of the variance), using either its raw or de-trended form (Fig. 6b, d). If these non-superchρον data are considered alone, the best match to the V15 SAF is found with an SAF lead of 120–125 Ma, similar to that determined for the M16 SAF. Therefore, both SAF models suggest that the relationship of the subduction flux to reversal rates may differ in form between superchρον and non-superchρον intervals. This might be expected based on the threshold-like character of controls

driving the modelled geodynamo into and out of superchrons (Olson and Amit, 2015; Hounslow, 2016).

4.1. Subduction flux proxies

If the subduction flux proxies indeed adequately track the true subduction flux, then their cross-correlation against LS reversal rates could provide additional insight. Lagged cross-correlations between the detrital zircon age frequency and the LS reversal rate reveals a statistically significant correlation with the zircon age frequency leading the reversal rate by 95–105 Ma (Fig. 8a). This is ~15–25 Ma less than the delay observed between the reversal rates and the SAF, which can be ascribed to the additional ‘crystallization delay’ described above. Unravelling these correlations at a 100 Ma lead reveals that this relationship is largely driven by the superchρον to non-superchρον transitions in the LS reversal rates, and is perturbed by outlier points in the LS reversal rates in the latest Devonian–Early Carboniferous (365–325 Ma) and Late Jurassic (170–160 Ma; Fig. 8b).

Cross-correlation of the Sr proxy and the LS reversal rate yields a marginally non-significant correlation with the Sr proxy leading the reversal rate by 105–125 Ma (Fig. 8c). The unravelling of this relationship (using a lead of 120 Ma) shows that it too is largely driven by the difference between superchρον and non-superchρον states in the age interval 0–265 Ma; the age interval with the most complete data. Much of the data in the interval 330–375 Ma are outliers with respect to this relationship (Fig. 8d). Considered alone, the LS reversal rate data from the non-superchρον intervals is best correlated to the Sr proxy with a lead (of the latter) of 150 Ma, but again the estimated data points for the latest Devonian–Early Carboniferous (365–325 Ma) remain outliers to this relationship.

4.2. Cyclicity in fluxes and reversal rates

An alternative way to assess similarity among time series is to look for comparable cyclical behaviour via autocorrelation. Cyclical variations in the LS reversal rates are strong at around a 190 Ma period (Fig. 9a), which clearly corresponds to the repeat interval of the

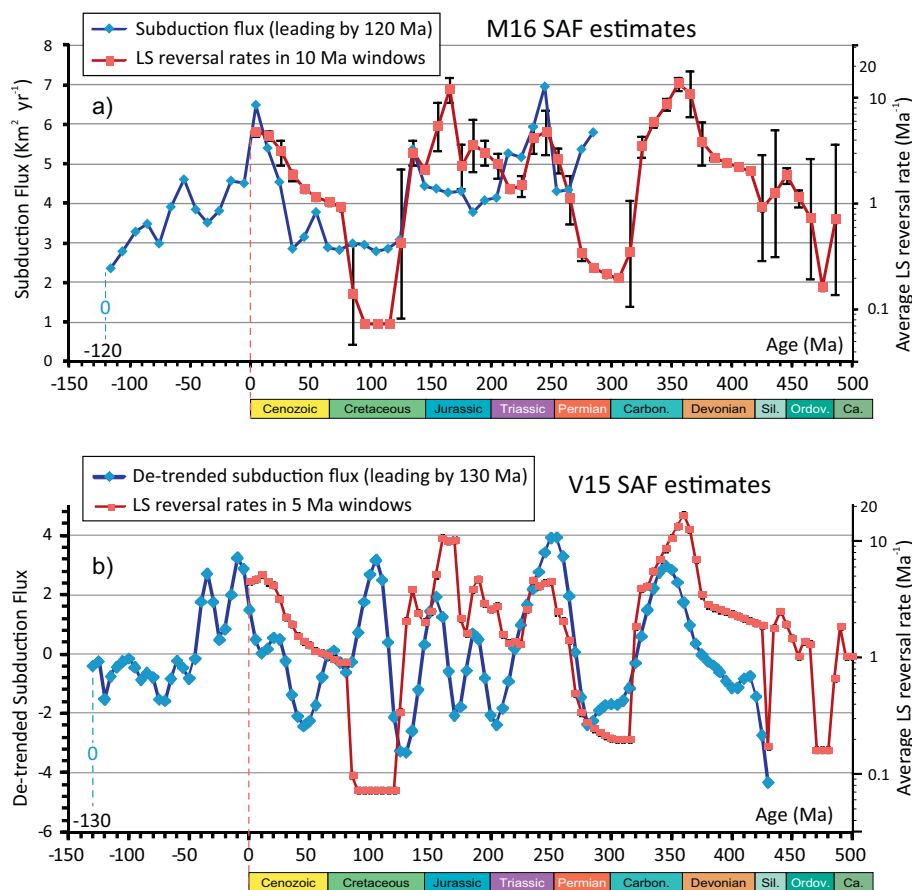


Fig. 7. a) Comparison of the M16 SAF and LS reversal rate with a 120 Ma SAF lead. LS reversal rates were determined at 10 Ma intervals to be scaled equally to that of the M16 SAF. The timescale is paired with the LS reversal rate timescale. Error bars on the reversal rate data are 1 σ standard deviations of the 1 Ma LS reversal rates in each 10 Ma window. The M16 SAF is raw in this comparison (not de-trended). b) Comparison of the de-trended V15 SAF and LS reversal rate with a 130 Ma SAF lead.

superchrons and the reversal rate recovery following them for some 30–50 Ma duration (Fig. 7a). The M16 SAF shows a period at ~230 Ma that is primarily driven by the similar intervals of decreasing flux between 370–240 Ma and 130–0 Ma (Figs. 1, 9b). For the V15 SAF, the strongest positive period is at 250–255 Ma, which relates to the lows in the flux at around 170 Ma and 420 Ma and the adjacent highs at around 130 Ma and 380 Ma (Figs. 1, 9c). Although these cyclicities (190, 230 and 250 Ma) do not exactly correspond, they are all broadly similar to a dominant timescale observed in geodynamic models (Coltice et al., 2013). It is also important to note that autocorrelation will only detect self-harmonic trends (that may or may not be linked between a pair of processes), and therefore cannot identify non-harmonic correlations between processes that may otherwise be significant.

4.3. Predictive capacity of the subduction flux estimates

Unravelling of the correlation relationships has suggested that there is some merit in considering the differences in LS reversal rates between superchrons and the reversing state (as largely expressed in the cross-correlations; Figs. 5, 6, 8), but also in considering the non-superchron reversal rate data independently from the superchron state data. This is also justified by the fact that reversing state data has a greater data density, whereas that from the superchrons is rather sparse. With this and the time-leads discussed in Section 3.1, we used multiple linear regression to explore the capacity to model the LS reversal rates using the subduction flux estimates (M16 and V15 SAF) and proxies (detrital zircon and Sr proxies) (Table 3). This is informed by assessment of statistical relative importance (Grömping, 2006). This analysis suggests that the SAF (from either M16 or V15) is most powerfully expressed in the non-superchron dataset, and like the previous qualitative assessments, it demonstrates that the M16 SAF is more strongly related to the LS reversal rate than the V15 SAF. The detrital zircon and Sr proxies are

a stronger influence on the predictions when all the data is considered together, indicating these principally express variance in the superchron to reversing state cycles.

5. Discussion

Our analysis has uncovered a statistically significant, positive correlation between the M16 SAF and a new time series of log LS reversal rates, with a delay time of 120 Ma (SAF leading). A positive correlation is also found between the V15 SAF and the log of LS reversal rates with a delay time of 130 Ma, but independent subduction flux proxies (detrital zircon age frequency or the 'mantle' Sr flux) question the veracity of the V15 SAF prior to ~180 Ma. Cross-correlations between the subduction proxies and the time series of reversal rates further corroborate the temporal relationships suggested by the M16 SAF-reversal rate cross-correlations. Unravelling these relationships at the time leads suggested by the cross-correlation reveals that much of the unexplained variance is related to time intervals with 'outliers' and an apparently differing response between superchron and non-superchron states. Autocorrelation of the SAF and reversal rates recovers strong periodicities close to the characteristic timescale of mantle convection derived from geodynamic models (~200 Ma; Coltice et al., 2013), but not otherwise identical.

What do these correlations and delay times mean? Before considering this important question, we acknowledge that we should probably expect no more than a weak relationship between reported changes in the global subduction flux at the surface and geomagnetic field behaviour generated by processes in the core, for a variety of reasons.

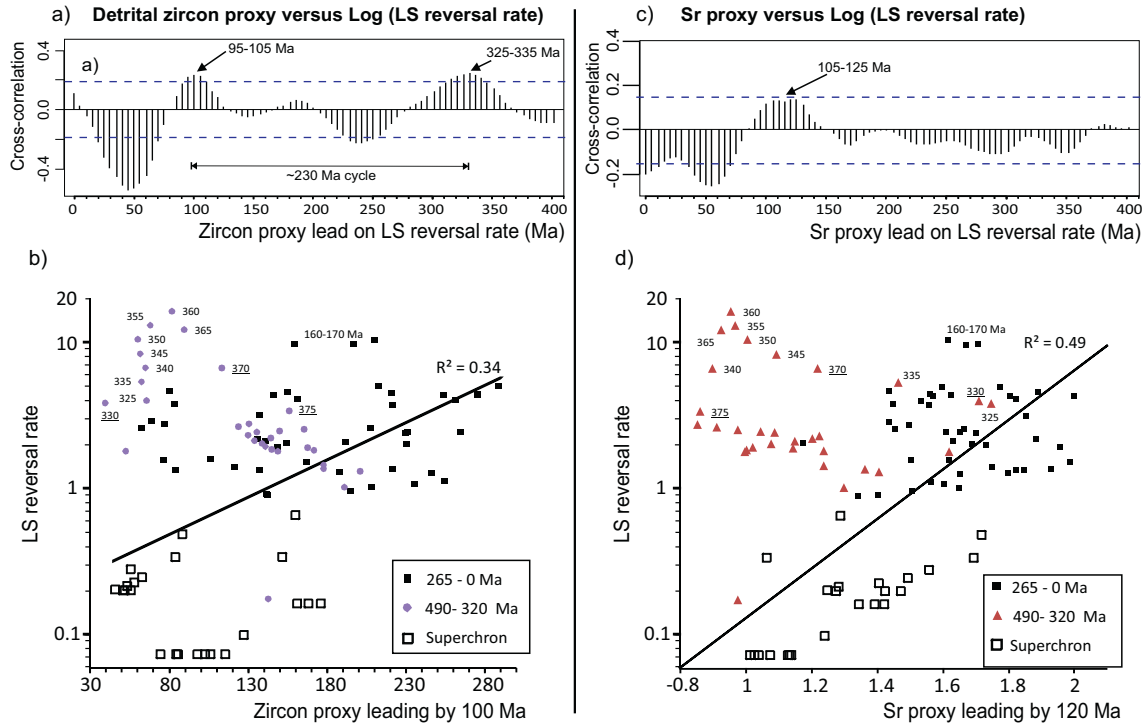


Fig. 8. a) Cross-correlation between the detrital zircon subduction flux proxy and LS reversal rates; c) cross-correlation between the Sr subduction flux proxy and LS reversal rates. The cross-correlations in a) and c) use both superchiron and non-superchiron data. Dashed blue lines indicate the 5% significance level. b) and d) show instantaneous comparisons of these correlations with a zircon proxy lead of 100 Ma, and a Sr proxy lead of 120 Ma, respectively. Data in these comparisons are separated into points from superchiron and non-superchiron intervals. The black lines show linear regressions using data from 0 to 315 Ma (both superchiron and non-superchiron data), which yield the best positive correlations close to the cross-correlation peaks observed in panels a) and c). Select outlier points are labelled with age in Ma. In the 375–325 Ma range those underlined are based on actual magnetostratigraphic data, and ages not underlined are based on reversal rate interpolations across intervals with missing data. (For interpretation of the references to color in this figure legend, the reader is referred to the web version of this article.)

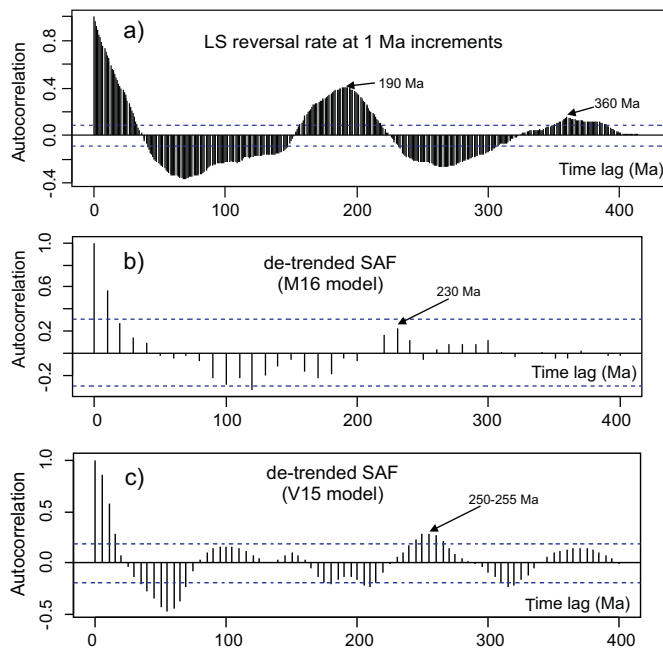


Fig. 9. a) Autocorrelation of the LS reversal rates at 1 Ma increments, showing the ~190 Ma cyclicality in the reversal rates and its multiple at around 360 Ma ($n = 493$). b) Autocorrelation of the M16 derived SAF at 10 Ma increments ($n = 41$). c) Autocorrelation of the V15 SAF at 5 Ma intervals ($n = 115$). Blue dashed lines indicate the 5% significance level. The peak near 0 Ma lag is due to the self-similarity at small lags. (For interpretation of the references to color in this figure legend, the reader is referred to the web version of this article.)

5.1. Assessment of deficiencies

Firstly, there are some large uncertainties and significant deficiencies in both the plate models from which the SAF estimates are derived, and in parts of the geomagnetic polarity timescale from which the reversal rates are calculated. The V15 and M16 SAF curves and the subduction flux proxies are all in reasonable agreement back to the Early Jurassic (~180 Ma), but prior to that time the V15 and M16 SAF curves are largely dissimilar. Perhaps unsurprisingly, the Early Jurassic marks the time when plate models become entirely reliant on synthetic oceanic lithosphere, such that deviations between models (and from reality) are prone to magnify from this point. The detrital zircon age frequency and 'mantle' Sr flux ratio suggest that the M16 SAF curve is more reliable than the V15 SAF estimates for pre-Early Jurassic time, but the M16 SAF extends only back to 410 Ma and prior to that the subduction flux proxies themselves exhibit dissimilar trends. Likewise, the geomagnetic polarity timescale constructed here becomes significantly more uncertain prior to ~320 Ma, before which time most of the timescale must be modelled. The mid-Jurassic reversal rates may also be biased toward higher rates, due to the inclusion of deep-tow sea floor anomaly data (Fig. 3); a possibility which needs a more detailed assessment using the land-based datasets (Gipe, 2013). Nevertheless, the positive cross-correlation of the M16 SAF and reversal rate at a lag of 120 Ma falls within the time frame for which both the plate model and geomagnetic timescale are reasonably well known.

Secondly, the SAF curves do not represent volume or thermal mass, which would be the ideal indices for comparison. The subduction of old (thicker and colder) oceanic lithosphere is likely to have a greater influence on CMB heat flow than the subduction of young (thinner, warmer) oceanic lithosphere. Variable sinking speeds related to differing slab properties, slab stagnation at the transition zone, and the

Table 3

Capacity to predict the LS reversal rate using subduction area flux estimates and the Zr and Sr subduction flux proxies. Data based on multiple linear regression, performed in R. pVar is the percentage of variance explained by the regression model, n = number of data. Relative importance to the regression model is based on the *lm*g statistic (Grömping, 2006), after Lindeman, Merenda, and Gold. Age interval is the age start and end of the overlapping datasets, when the leads are applied, in terms of the age steps for the SAF models. ^Q = quadratic, rather than linear used in regression, based on a visual assessment of best fit to the LS reversal rate. M16, V15 data used are the detrended flux model estimates, Zr=Zr proxy, Sr=Sr mantle proxy. ‘–’ on relative importance indicates, the sign on the coefficient is negative (i.e. negative contribution to LS reversal flux).

Model. Data	Age interval	Lead on proxy [Ma]	pVar, n	Relative importance [%]
SAF-M16. All	405–125 Ma	M16[+ 120], Zr[+ 100], Sr[+ 120]	57.6, 29	M16[31] ^Q , Zr[25], Sr[44]
SAF-M16. Non-superchron	385–125 Ma	M16[+ 120], Zr[+ 100], Sr[+ 120]	30.4, 22	M16[87] ^Q , –Zr[6], –Sr[7]
SAF-V15. All	560–120 Ma	V15[+ 120], Zr[+ 100], Sr[+ 120]	13.3, 89	V15[27], Zr[56], Sr[17]
SAF-V15. Non-superchron	560–120 Ma	V15[+ 120], Zr[+ 100], Sr[+ 120]	32.9, 70	V15[92], –Zr[4], –Sr[4]

regional prehistory of the lower mantle will also complicate the association between the true (volumetric) subduction flux and time-dependent changes to the CMB heat flow. Nevertheless, we note that the concept of a first-order, globally-averaged, mean sinking rate appears defensible from the outcome of subduction-tomography relationships (van der Meer et al., 2010, 2018; Domeier et al., 2016).

Thirdly, the complex and poorly understood dynamics of both the lowermost mantle (Torsvik et al., 2016) and the geodynamo process may confound attempts to produce a one-to-one relationship between any single paleomagnetic dataset and any single surface process that can affect the deep mantle. One expression of this is that although numerical dynamo simulations have indicated that the relationship between reversal frequency and CMB heat flow should be positive; regardless of whether the heat flow is homogeneous around the CMB or has a heterogeneous pattern (Olson and Amit, 2014), the nature of the scaling relationships between the two are unknown because of limitations in the models and in our knowledge of how to constrain them. These scaling relationships likely influence the dramatic reversal rate change into and out of superchrons, so the necessarily continuous subduction process is unlikely to follow the geodynamo reversal process in a linear way. Our analysis tries to express some of this in the way we separate superchron and non-superchron datasets. Another expression of this complexity is that geodynamo models suggest polarity reversal rates likely respond to lower mantle heat flow and its spatial inequality (Olson and Amit, 2014), whereas our one dimensional analysis has averaged out any spatial inequality. This is further complicated by the occurrence of true polar wander, which will rotate any such subduction-imposed, lower mantle heat-flux pattern in the reference frame of the geodynamo. Still, even if the relationship is non-linear and complicated by spatial variations, changes to the subduction flux will generally induce changes to the CMB heat flux, and so the geodynamo.

Finally, deep mantle-lithosphere feedbacks may confound correlations between surface tectonics and geomagnetic field behaviour, because subduction dynamics at the surface may not necessarily lead changes occurring in the deep Earth (Torsvik et al., 2016). In this paper we explicitly explore the question of whether the time-dependent subduction flux modulates the geodynamo, but deep mantle dynamics could potentially also independently alter the CMB heat flux. For example, reversal rate variations in the Jurassic-Cretaceous have been linked with plumes and ‘superplumes’ (Biggin et al., 2012; Amit and Olson, 2015; Li et al., 2018), as well as episodes of true polar wander (Biggin et al., 2012). Yet mantle plumes, when they ultimately arrive at the surface, can also trigger significant changes to plate kinematics (Buiter and Torsvik, 2014) and thus alter the subduction flux. Because the departure of a mantle plume can modify the CMB heat flux before the plume arrives at the surface, changes in the geomagnetic field may thus *predate* global tectonic changes, in addition to being driven by them. Thus, both the subduction flux and ‘plume flux’ are expected to modulate the CMB heat flux, but also one another, blurring the distinction between ‘forcing’ and ‘response’ and potentially producing periodic behaviour (Li et al., 2018). Thus, with respect to the geodynamo’s forcing, the subduction flux is only one of several components of

a complex system containing important feedbacks. However, because sinking slabs (as the principal source of buoyancy in the mantle) are the primary driver of mantle convection, we expect that the subduction flux has played a dominating role in modulating the CMB heat flux, and thus that the positive correlation between the SAF and reversal rate time series is foremost driven by a subduction flux lead.

5.2. Subduction-related timing delays in the mantle

With the aforementioned caveats in mind, we return to the question: what could the delay times between the SAF and reversal rate mean? According to the contention that the subduction flux lead is the most likely to be physically meaningful, we here focus on the ~120 Ma time delay with the reversal rates following the subduction flux (Fig. 10). So what could the 120 Ma lag between subduction flux and geomagnetic field response mean in terms of physical processes? One simple interpretation would be that the 120 Ma delay effectively represents the average transit time for a subducting slab to sink through the mantle. In this case, the heat flux at the CMB would be modified by the physical arrival of relatively cold lithospheric slabs that would enhance the thermal gradient across the CMB at specific locations. Locally, the thermal diffusivity of slabs could also be strongly augmented by the post-perovskite phase change that can occur in the lowermost mantle (Lay et al., 2008; Hunt et al., 2012). However, comparisons between paleogeographic models and seismic tomographic models reveal that slabs take at least 150 Ma to transit through the mantle, and probably more often between 200 and 300 Ma (van der Meer et al., 2010, 2018; Domeier et al., 2016). Given that a further delay of some millions to tens of millions of years may be required following a change to the CMB heat flux before the geodynamo responds (due to stratification in the outermost core; Buffett, 2015), it seems unlikely that the 120 Ma delay time reflects the whole mantle transit time of slabs.

On the other hand, a sinking slab and the thermal anomaly associated with it may not necessarily need to physically encounter the CMB in order for it to exert a change to the CMB heat flux. The sinking of a slab could potentially setup a convective cell that thins the thermal boundary layer (just above the CMB) before it physically arrives (Biggin et al., 2012). In this context, geodynamic studies attempting to link surface dynamics with consequent changes to CMB heat flow have predicted that the delay time between such phenomena should be 30–60 Ma (Bunge et al., 2003; Buffett, 2015; Biggin et al., 2012; Zhang and Zhong, 2011). This is considerably shorter than both seismologically-constrained whole-mantle slab transit times (~150–300 Ma) and also our observed lag time (~120 Ma).

van der Meer et al. (2018) found that slabs sinking through the lower mantle appear to progressively decelerate down to a depth of ~1500 km, whereupon their sinking rates increase again as they transit the lowermost mantle below. They interpret this deceleration zone to be a consequence of increasing mantle viscosity (possibly related to the increasing strength of ferropericlase; Marquardt and Miyagi, 2015), which they infer to decrease again below 1500 km. With use of a globally-averaged, whole mantle slab sinking rate of ~1.2 cm/yr (van

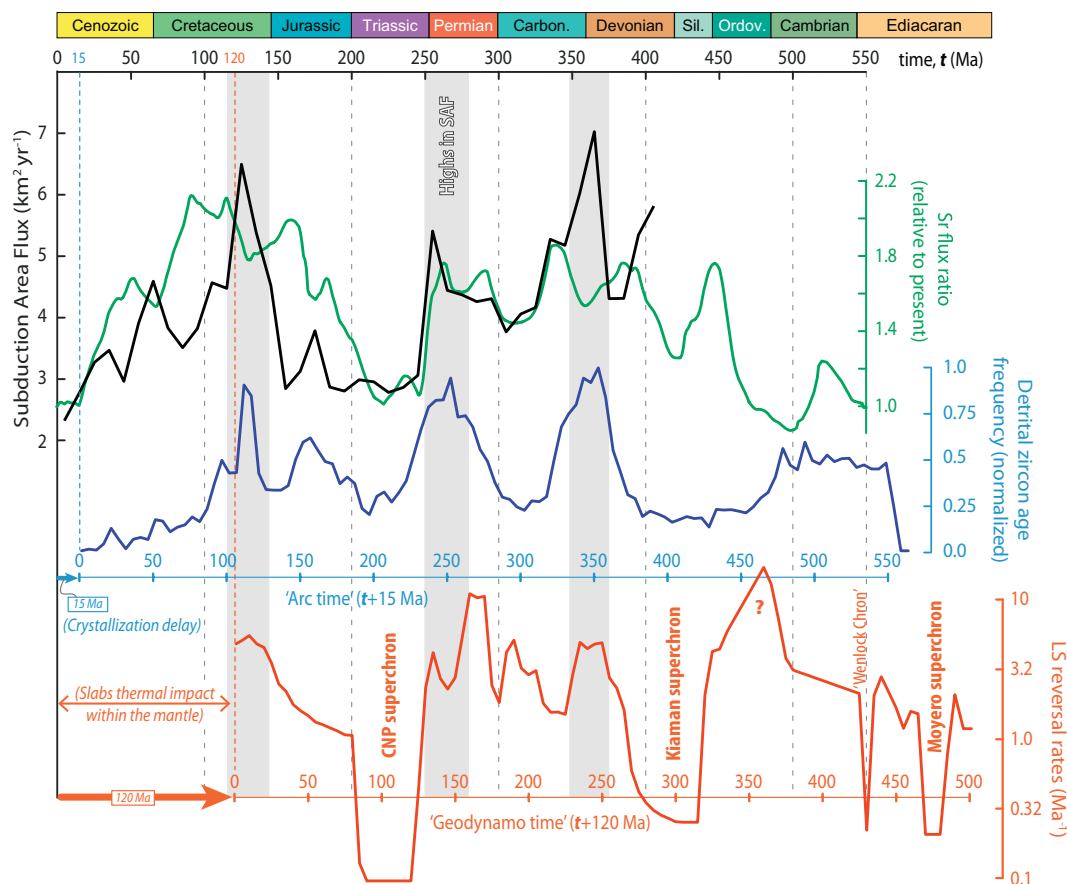


Fig. 10. Summary diagram showing the M16 SAF (black line), the Sr proxy of van der Meer et al. (2017) (green line), the detrital zircon proxy (blue line) and the LS reversal rates (red line). The M16 and Sr proxy are tied to the timescale at the top of the figure (time = t). The detrital zircon proxy is offset by 15 Ma according to the crystallization delay (blue 'Arc' timescale, time = $t + 15$ Ma). The LS reversal rate is offset by 120 Ma according to the lags reported in this paper, and so follows the red 'Geodynamo' timescale (time = $t + 120$ Ma). Dashed blue and red vertical lines show the offset of these 'Arc' and 'Geodynamo' timescales, respectively. Grey vertical bars highlight times when the SAF is relatively high. (For interpretation of the references to color in this figure legend, the reader is referred to the web version of this article.)

der Meer et al., 2010, 2018), a slab should reach ~ 1500 km by 125 Ma. The coincidence of this transit time with the observed lag time between the SAF and reversal rates could suggest that convective 'sweeping' of the lowermost mantle thermal boundary layer can only be induced by sinking slabs once they penetrate this lower mantle 'deceleration zone', and enter the zone of relatively lower viscosity below.

Recent attempts to couple numerical mantle models to inputs of core models either directly (Olson et al., 2013) or indirectly (Choblet et al., 2016) have yielded less than clear results. This is in large part due to our poor understanding of various parameters of both the mantle and core, as well as the timescales involved with their forcings and feedbacks. Our results here present new insight into these timescales, and provide new constraints for linked numerical mantle-core models and numerical investigations of the connections between surface and deep Earth heat fluxes. Our findings also suggest that the lower mantle 'deceleration zone' of van der Meer et al. (2018) may be of particular importance to lower mantle dynamics, and deserves further attention.

6. Conclusions

Based on numerical dynamo simulations and first-order mantle dynamical arguments, it is expected that some time-lagged, positive correlation exists between the global flux of subducting lithosphere and temporal variations in the geomagnetic reversal rate. New model-derived and observational data to test this hypothesis have been evaluated and found to show that such a relationship can be demonstrated through the Phanerozoic, with a time lag of ~ 120 Ma (subduction flux

leading reversal rate). This lag of 120 Ma is thus interpreted to represent the average effective relay time to transmit thermal information from the surface to the core-mantle boundary, which is faster than tomographically determined whole-mantle slab sinking rates but also slower than previous estimates of this relay time derived from geodynamic models. However, a range of likely confounding factors have also been identified, which may complicate this relationship. Future work will be required to cement the conclusions formulated here, and in particular to further probe the nature of the ~ 120 Ma lag, but these results nevertheless present important new constraints for the next generation of geodynamical models.

Acknowledgements

MWH and AJB acknowledge NERC Standard grant NE/P00170X/1. MD acknowledges support from the Research Council of Norway, through RCN project 250111. AJB acknowledges his reading of Eide and Torsvik (1996) nearly twenty years ago, and many discussions with Trond Torsvik since, in providing the motivation and interest to pursue tectonic explanations for long-timescale variations in geomagnetic reversal frequency. We thank Douwe van der Meer and an anonymous reviewer for providing feedback that greatly improved the manuscript, and we also thank Douwe van der Meer for providing the Sr curve used in Figs. 1 and 10.

Author contributions

MWH compiled the reversal rate record, performed the time series analysis, and wrote the manuscript. MD compiled the subduction flux records and wrote the paper. AJB instigated the study, provided initial proof of concept of a ~120 Myr time delay, and wrote the paper.

Appendix A. Supplementary data

Supplementary data to this article can be found online at <https://doi.org/10.1016/j.tecto.2018.05.018>.

References

- Agard, P., Jolivet, L., Vrielynck, B., Burov, E., Monié, P., 2007. Plate acceleration: the obduction trigger? *Earth Planet. Sci. Lett.* 258, 428–441.
- Agard, P., Yamato, P., Jolivet, L., Burov, E., 2009. Exhumation of oceanic blueschists and eclogites in subduction zones: timing and mechanisms. *Earth Sci. Rev.* 92, 53–79.
- Allègre, C.J., Louvat, P., Gaillardet, J., Meynadier, L., Rad, S., Capmas, F., 2010. The fundamental role of island arc weathering in the oceanic Sr isotope budget. *Earth Planet. Sci. Lett.* 292, 51–56.
- Amit, H., Olson, P., 2015. Lower mantle superplume growth excites geomagnetic reversals. *Earth Planet. Sci. Lett.* 414, 68–76.
- Aubert, J., Labrosse, S., Poitou, C., 2009. Modelling the palaeo-evolution of the geodynamo. *Geophys. J. Int.* 179, 1414–1428.
- Barth, A.P., Wooden, J.L., Jacobson, C.E., Economos, R.C., 2013. Detrital zircon as a proxy for tracking the magmatic arc system: the California arc example. *Geology* 41, 223–226.
- Bazhenov, M.L., Levashova, N.M., Meert, J.G., Golovanova, I.V., Danukalov, K.N., Fedorova, N.M., 2016. Late Ediacaran magnetostratigraphy of Baltica: evidence for magnetic field hyperactivity? *Earth Planet. Sci. Lett.* 435, 124–135.
- Becker, R.T., Gradstein, F.M., Hammer, O., 2012. The Devonian Period. In: Gradstein, F.M., Ogg, J.G., Schmitz, M.D., Ogg, G.M. (Eds.), *The Geologic Time Scale 2012*. Elsevier, pp. 559–602.
- Biggin, A.J., Steinberger, B., Aubert, J., Suttie, N., Holme, R., Torsvik, T.H., van der Meer, D.G., van Hinsbergen, D.J.J., 2012. Possible links between long-term geomagnetic variations and whole-mantle convection processes. *Nat. Geosci.* 5, 526–533.
- Buffett, B.A., 2015. Core-mantle interactions. In: Olson, P. (Ed.), *Core Dynamics*. Elsevier, Amsterdam, pp. 213–224.
- Buiter, S.J.H., Torsvik, T.H., 2014. A review of Wilson Cycle plate margins: a role for mantle plumes in continental break-up along sutures? *Gondwana Res.* 26, 627–653.
- Bunge, H.P., Hagelberg, C.R., Travis, B.J., 2003. Mantle circulation models with variational data assimilation: inferring past mantle flow and structure from plate motion histories and seismic tomography. *Geophys. J. Int.* 152, 280–301.
- Cawood, P.A., Hawkesworth, C.J., Dhuime, B., 2012. Detrital zircon record and tectonic setting. *Geology* 40, 875–878.
- Choblet, G., Amit, H., Hussong, L., 2016. Constraining mantle convection models with palaeomagnetic reversals record and numerical dynamos. *Geophys. J. Int.* 207, 1165–1184.
- Cogné, J.-P., Humler, E., 2004. Temporal variation of oceanic spreading and crustal production rates during the last 180 My. *Earth Planet. Sci. Lett.* 227, 27–439.
- Coltice, N., Seton, M., Rolf, T., Müller, R.D., Tackley, P.J., 2013. Convergence of tectonic reconstructions and mantle convection models for significant fluctuations in seafloor spreading. *Earth Planet. Sci. Lett.* 383, 92–100.
- Condie, K.C., Arndt, N., Davaille, A., Puetz, S.J., 2017. Zircon age peaks: production or preservation of continental crust? *Geosphere* 13, 227–234.
- Conrad, C.P., 2013. The solid Earth's influence on sea level. *GSA Bull.* 125, 1027–1052.
- Constable, C., 2000. On rates of occurrence of geomagnetic reversals. *Phys. Earth Planet. Inter.* 118, 181–193.
- Constable, C., Johnson, C.L., 2005. A paleomagnetic power spectrum. *Phys. Earth Planet. Inter.* 153, 61–73.
- Courtillot, V., Olson, P., 2007. Mantle plumes link magnetic superchrons to Phanerozoic mass depletion events. *Earth Planet. Sci. Lett.* 260, 495–504.
- Cowpertwait, P.S.P., Metcalfe, A.V., 2009. *Introductory Time Series Analysis With R*. Springer, Dordrecht.
- Cox, A., 1968. Lengths of geomagnetic polarity intervals. *J. Geophys. Res.* 73, 3247–3260.
- Didenko, A.N., 2011. Possible causes of quasi-periodic variations in geomagnetic reversal frequency and 87Sr/86Sr ratios in marine carbonates through the Phanerozoic. *Russ. Geol. Geophys.* 52, 1530–1538.
- Dilek, Y., Furnes, H., 2011. Ophiolite genesis and global tectonics: geochemical and tectonic fingerprinting of ancient oceanic lithosphere. *GSA Bull.* 123, 387–411.
- Domeier, M., Torsvik, T.H., 2014. Plate tectonics in the late Paleozoic. *Geosci. Front.* 5, 303–350.
- Domeier, M., Torsvik, T.H., 2018. Full-plate modelling in pre-Jurassic time. *Geol. Mag.* <https://doi.org/10.1017/S0016756817001005>.
- Domeier, M., Doubrovine, P.V., Torsvik, T.H., Spakman, W., Bull, A.L., 2016. Global correlation of lower mantle structure and past subduction. *Geophys. Res. Lett.* 43, 4945–4953.
- Driscoll, P., Olson, P., 2009. Effects of buoyancy and rotation on the polarity reversal frequency of gravitationally driven numerical dynamos. *Geophys. J. Int.* 178, 1337–1350.
- Dziewonski, A.M., Lekic, V., Romanowicz, B.A., 2010. Mantle anchor structure: an argument for bottom up tectonics. *Earth Planet. Sci. Lett.* 299, 69–79.
- Eide, E.A., Torsvik, T.H., 1996. Paleozoic supercontinental assembly, mantle flushing, and genesis of the Kiaman Superchron. *Earth Planet. Sci. Lett.* 144, 389–402.
- Gaffin, S., 1987. Ridge volume dependence on seafloor generation rate and inversion using long term sealevel change. *Am. J. Sci.* 287, 596–611.
- Gallet, Y., Courtillot, V., 1995. Geomagnetic reversal behaviour since 100 Ma. *Phys. Earth Planet. Inter.* 92, 235–244.
- Gallet, Y., Hulot, G., 1997. Stationary and nonstationary behaviour within the geomagnetic polarity time scale. *Geophys. Res. Lett.* 24, 1875–1878.
- Gallet, Y., Pavlov, V.E., 2016. Three distinct reversing modes in the geodynamo. *Izv. Phys. Solid Earth* 52, 291.
- Gallet, Y., Pavlov, V., Courtillot, V., 2003. Magnetic reversal frequency and apparent polar wander of the Siberian Platform in the earliest Palaeozoic, inferred from the Khorbusuonka River section (northeastern Siberia). *Geophys. J. Int.* 154, 829–840.
- Gipe, R.A., 2013. Callovian (Upper Middle Jurassic) Magnetostratigraphy: A Composite Polarity Pattern From France, Britain and Germany, and Its Correlation to the Pacific Marine Magnetic Anomaly Model. Purdue University (Unpubl. Msc.).
- Glatzmaier, G.A., Coe, R.S., Hongre, L., Roberts, P.H., 1999. The role of the Earth's mantle in controlling the frequency of geomagnetic reversals. *Nature* 401, 885–890.
- Goddéris, Y., François, L.M., 1995. The Cenozoic evolution of the strontium and carbon cycles: relative importance of continental erosion and mantle exchanges. *Chem. Geol.* 126, 169–190.
- Gold, T., 1955. Instability of the earth's axis of rotation. *Nature* 175, 526–529.
- Gradstein, F.M., Ogg, J.G., Schmitz, M., Ogg, G. (Eds.), 2012. *The Geologic Time Scale 2012*. Elsevier, Amsterdam.
- Gradstein, F.M., Ogg, J.G., Smith, A.G., Bleeker, W., Lourens, L.J., 2004. A new geologic time scale, with special reference to Precambrian and Neogene. *Episodes* 27, 83–100.
- Grömping, U., 2006. Relative importance for linear regression in R: the package relaimpo. *Journal of statistical software* 17, 1–27.
- Hansma, J., Tohver, E., Yan, M., Trinajstić, K., Roelofs, B., Peek, S., Hocking, R., 2015. Late Devonian carbonate magnetostratigraphy from the Oscar and Horse Spring Ranges, Lennard Shelf, Canning Basin, Western Australia. *Earth Planet. Sci. Lett.* 409, 232–242.
- Haq, B.U., Schutter, S.R., 2008. A chronology of Paleozoic sea-level changes. *Science* 322, 64–68.
- Hounslow, M.W., 2016. Geomagnetic reversal rates following Palaeozoic superchrons have a fast restart mechanism. *Nat. Commun.* 7. <http://dx.doi.org/10.1038/ncomms12507>.
- Hounslow, M.W., Balabanov, Y.P., 2016. A geomagnetic polarity timescale for the Permian, calibrated to stage boundaries. In: Lucas, S.G., Shen, S.-Z. (Eds.), *The Permian Timescale*. Geological Society, London, Special Publications, vol. 450 <http://dx.doi.org/10.1144/SP450.8>.
- Hounslow, M.W., Muttoni, G., 2010. The geomagnetic polarity timescale for the Triassic: linkage to stage boundary definitions. In: Lucas, S.G. (Ed.), *The Triassic Timescale*. Geological Society, London, Special Publications, vol. 334. pp. 61–102.
- Hughes, G.R., Mahood, G.A., 2008. Tectonic controls on the nature of large silicic calderas in volcanic arcs. *Geology* 36, 627–630.
- Hulot, G., Gallet, Y., 2003. Do superchrons occur without any palaeomagnetic warning? *Earth Planet. Sci. Lett.* 210, 191–201.
- Hunt, S.A., Davies, D.R., Walker, A.M., McCormack, R.J., Wills, A.S., Dobson, D.P., Li, L., 2012. On the increase in thermal diffusivity caused by the perovskite to post-perovskite phase transition and its implications for mantle dynamics. *Earth Planet. Sci. Lett.* 319, 96–103.
- Idnurm, G., Klootwijk, C., Théveniaut, H., Trench, A., 1996. Magnetostratigraphy. In: Young, G.C., Laurie, J.R. (Eds.), *The Australian Phanerozoic Timescale*. Oxford University Press, pp. 23–51.
- James, G., Witten, D., Hastie, T., 2013. Introduction to statistical learning, with applications in R. In: Springer Texts in Statistics, vol. 103 Springer, Amsterdam.
- Jones, C.E., Jenkyns, H.C., Coe, A.L., Stephen, H.P., 1994. Strontium isotopic variations in Jurassic and Cretaceous seawater. *Geochim. Cosmochim. Acta* 58, 3061–3074.
- Kent, D.V., Olsen, P., Muttoni, G., 2017. Astrochronostratigraphic polarity time scale (APTS) for the Late Triassic and Early Jurassic from continental sediments and correlation with standard marine stages. *Earth Sci. Rev.* 166, 153–180.
- Kirschvink, J.L., Magaritz, M., Ripperdan, R.L., Zhuravlev, A.Y., Rozanov, A.Y., 1991. The Precambrian-Cambrian boundary: magnetostratigraphy and carbon isotopes resolve correlation problems between Siberia, Morocco, and South China. *GSA Today* 1 (4), 69–91 (April).
- Kwiatkowski, D., Phillips, P.C.B., Schmidt, P., Shin, Y., 1992. Testing the null hypothesis of stationarity against the alternative of a unit root. *J. Econ.* 54, 159–178.
- Lanik, A., Over, D.J., Schmitz, M., Kirchgasser, W.T., 2016. Testing the limits of chronostratigraphic resolution in the Appalachian Basin, Late Devonian (middle Frasnian), eastern North America: new U-Pb zircon dates for the Belpre Tephra suite. *Geol. Soc. Am. Bull.* 128, 1813–1821.
- Larson, R.L., Olson, P., 1991. Mantle plumes control magnetic reversal frequency. *Earth Planet. Sci. Lett.* 107, 437–447.
- Lay, T., Hernlund, J., Buffett, B.A., 2008. Core-mantle boundary heat flow. *Nat. Geosci.* 1, 25–32.
- Li, M., Ogg, J., Zhang, Y., Huang, C., Hinnov, L., Chen, Z.Q., Zou, Z., 2016. Astronomical tuning of the end-Permian extinction and the Early Triassic Epoch of South China and Germany. *Earth Planet. Sci. Lett.* 441, 10–25.
- Li, M., Zhong, S.J., Olson, P., 2018. Linking lowermost mantle structure, core-mantle boundary heat flux and mantle plume formation. *Phys. Earth Planet. Inter.* 277, 10–29.
- Loader, C., 1997. Locfit: an introduction. *Stat. Comput. Graph. Newsl.* 8, 11–17.
- Loader, C., 1999. *Local Regression and Likelihood*. Springer, Berlin.

- Lowrie, W., Kent, D.V., 2004. Geomagnetic polarity timescales and reversal frequency regimes. In: Channell, J.E.T., Kent, D.V., Lowrie, W., Meert, J. (Eds.), *Timescales of the Palaeomagnetic Field*. American Geophysical Union, pp. 117–129.
- Marquardt, H., Miyagi, L., 2015. Slab stagnation in the shallow lower mantle linked to an increase in mantle viscosity. *Nat. Geosci.* 8, 311–314.
- Matthews, K.J., Maloney, K.T., Zahirovic, S., Williams, S.E., Seton, M., Müller, R.D., 2016. Global plate boundary evolution and kinematics since the late Paleozoic. *Glob. Planet. Chang.* 146, 226–250.
- McFadden, P.L., Merrill, R.T., 1984. Lower mantle convection and geomagnetism. *J. Geophys. Res. Solid Earth* 89, 3354–3362.
- McFadden, P.L., Merrill, R.T., 1997. Asymmetry in the reversal rate before and after the Cretaceous Normal Polarity Superchron. *Earth Planet. Sci. Lett.* 149, 43–47.
- Miller, K.G., Kominz, M.A., Browning, J.V., Wright, J.D., Mountain, G.S., Katz, M.E., Sugarman, P.J., Cramer, B.S., Christie-Blick, N., Pekar, S.F., 2005. The Phanerozoic record of global sea-level change. *Science* 310, 1293–1298.
- Mills, B., Daines, S.J., Lenton, T.M., 2014. Changing tectonic controls on the long-term carbon cycle from Mesozoic to present. *Geochim. Geophys. Geosyst.* 15, 4866–4884.
- Mills, B.J.W., Scotese, C.R., Walding, N.G., Shields, G.A., Lenton, T.M., 2017. Elevated CO₂ degassing rates prevented the return of Snowball Earth during the Phanerozoic. *Nat. Commun.* 8, 1110. <http://dx.doi.org/10.1038/s41467-017-01456-w>.
- Molostovsky, E.A., Pechersky, D.M., Frolov, I.Y., 2007. The Phanerozoic magnetostratigraphic scale and its model on the basis of the cumulative distribution function. *Izv. Phys. Solid Earth* 43, 811–818.
- Moucha, R., Forte, A.M., Mitrovica, J.X., Rowley, D.B., Quere, S., Simmons, N.A., Grand, S.P., 2008. Dynamic topography and long-term sea-level variations: there is no such thing as a stable continental platform. *Earth Planet. Sci. Lett.* 271, 101–108.
- Müller, R.D., Seton, M., Zahirovic, S., Williams, S.E., Matthews, K.J., Wright, N.M., Shephard, G.E., Maloney, K.T., Barnett-Moore, N., Hosseini, M., Bower, D.J., Cannon, J., 2016. Ocean basin evolution and global-scale plate reorganization events since Pangea breakup. *Annu. Rev. Earth Planet. Sci.* 44, 107–138.
- Naidu, P.S., 1971. Statistical structure of geomagnetic field reversals. *J. Geophys. Res.* 76, 2649–2662.
- Ogg, J.G., 2012. Magnetostratigraphy. In: Gradstein, F.M., Ogg, J.G., Schmitz, M.D., Ogg, G.M. (Eds.), *The Geologic Time Scale 2012*. Elsevier, pp. 85–114.
- Olson, P.L., 2007. Gravitational dynamos and the low-frequency geomagnetic secular variation. *Proc. Natl. Acad. Sci.* 105, 20159–20166.
- Olson, P.L., Amit, H., 2014. Magnetic reversal frequency scaling in dynamos with thermochemical convection. *Phys. Earth Planet. Inter.* 229, 122–133.
- Olson, P., Amit, H., 2015. Mantle superplumes induce geomagnetic superchrons. *Front. Earth Sci.* <http://dx.doi.org/10.3389/feart.2015.00038>.
- Olson, P.L., Christensen, U.R., 2006. Dipole moment scaling for convection-driven planetary dynamos. *Earth Planet. Sci. Lett.* 250, 561–571.
- Olson, P.L., Coe, R.S., Driscoll, P.E., Glatzmaier, G.A., Roberts, P.H., 2010. Geodynamo reversal frequency and heterogeneous core-mantle boundary heat flow. *Phys. Earth Planet. Inter.* 180, 66–79.
- Olson, P.L., Deguen, R., Hinnov, L.A., Zhong, S.J., 2013. Controls on geomagnetic reversals and core evolution by mantle convection in the Phanerozoic. *Phys. Earth Planet. Inter.* 214, 87–103.
- Opdyke, N.D., Giles, P.S., Utting, J., 2014. Magnetic polarity stratigraphy and palynostratigraphy of the Mississippian-Pennsylvanian boundary interval in eastern North America and the age of the beginning of the Kiaman. *Geol. Soc. Am. Bull.* 126, 1068–1083.
- Pavlov, V., Gallet, Y., 2005. A third superchron during the Early Paleozoic. *Episodes—Newsmagazine of the International Union of Geological Sciences* 28, 78–84.
- Peng, S., Babcock, L.E., Cooper, R.A., 2012. The Cambrian Period. In: Gradstein, F.M., Ogg, J.G., Schmitz, M.D., Ogg, G.M. (Eds.), *The Geologic Time Scale 2012*, pp. 437–488.
- R Development Core Team, 2005. *R: A Language and Environment for Statistical Computing*. R Foundation for Statistical Computing, Vienna, Austria URL: <http://www.R-project.org> (ISBN 3-900051-07-0).
- Reyment, R.A., 1976. Geomagnetic reversal data statistically appraised. *Tectonophysics* 31, 73–91.
- Roberts, N.M.W., Spencer, C.J., 2015. The zircon archive of continent formation through time. In: Roberts, N.M.W., Van Kranendonk, M., Parman, S., Shirey, S., Clift, P.D. (Eds.), *Continent Formation Through Time*. Geological Society, London, Special Publications, vol. 389, pp. 197–225.
- Roda, M., Marotta, A.M., Spalla, M.I., 2010. Numerical simulations of an ocean-continent convergent system: influence of subduction geometry and mantle wedge hydration on crustal recycling. *Geochim. Geophys. Geosyst.* 11. <http://dx.doi.org/10.1029/2009GC003015>.
- Rodionov, V.P., 2016. Magnetostratigraphy of the Middle–Upper Cambrian Verkhnyaya Lena Group and Lower Ordovician Ust-Kut formation in the southern Siberian Platform. *Stratigr. Geol. Correl.* 24, 464–485.
- Rowley, D.B., 2002. Rate of plate creation and destruction: 180 Ma to present. *Geol. Soc. Am. Bull.* 114, 927–933.
- Schmidt, P.W., Williams, G.E., 2010. Ediacaran palaeomagnetism and apparent polar wander path for Australia: no large true polar wander. *Geophys. J. Int.* 182, 711–726.
- Seton, M., Müller, R.D., Zahirovic, S., Gaina, C., Torsvik, T., Shephard, G., Chandler, M., 2012. Global continental and ocean basin reconstructions since 200 Ma. *Earth Sci. Rev.* 113, 212–270.
- Shcherbakov, V., Fabian, K., 2012. The geodynamo as a random walker: a view on reversal statistics. *J. Geophys. Res. Solid Earth* 117. <http://dx.doi.org/10.1029/2011JB008931>.
- Shephard, G.E., Matthews, K.J., Hosseini, K., Domeier, M., 2017. On the consistency of seismically imaged lower mantle slabs. *Sci. Rep.* 7. <http://dx.doi.org/10.1038/s41598-017-11039-w>.
- Spasojevic, S., Gurnis, M., 2012. Sea level and vertical motion of continents from dynamic Earth models since the Late Cretaceous. *AAPG Bull.* 96, 2037–2064.
- Stampfli, G.M., Borel, G.D., 2002. A plate tectonic model for the Paleozoic and Mesozoic constrained by dynamic plate boundaries and restored synthetic oceanic isochrons. *Earth Planet. Sci. Lett.* 196, 17–33.
- Stampfli, G.M., Hochard, C., Vêrard, C., Wilhem, C., von Raumer, J., 2013. The formation of Pangea. *Tectonophysics* 593, 1–19.
- Steinberger, B.M., Torsvik, T.H., 2010. Toward an explanation for the present and past locations of the poles. *Geochim. Geophys. Geosyst.* 11. <http://dx.doi.org/10.1029/2009GC002889>.
- Steinberger, B.M., Torsvik, T.H., 2012. A geodynamic model of plumes from the margins of Large Low Shear Velocity Provinces. *Geochim. Geophys. Geosyst.* <http://dx.doi.org/10.1029/2011GC003808>.
- Tominaga, M., Tivey, M.A., Sager, W.W., 2015. Nature of the Jurassic magnetic Quiet Zone. *Geophys. Res. Lett.* 42, 8367–8372.
- Torsvik, T.H., Steinberger, B., Gurnis, M., Gaina, C., 2010. Plate tectonics and net lithosphere rotation over the past 150 My. *Earth Planet. Sci. Lett.* 291, 106–112.
- Torsvik, T.H., Van der Voo, R., Preeden, U., Mac Niocaill, C., Steinberger, B., Doubrovine, P.V., van Hinsbergen, D.J.J., Domeier, M., Gaina, C., Tohver, T., Meert, J., McCausland, P.J.A., Cocks, L.R.M., 2012. Phanerozoic polar wander, palaeogeography and dynamics. *Earth Sci. Rev.* 114, 325–368.
- Torsvik, T.H., Steinberger, B., Ashwal, L.D., Doubrovine, P.V., Trønnes, R.G., 2016. Earth evolution and dynamics—a tribute to Kevin Burke. *Can. J. Earth Sci.* 53, 1073–1087.
- Trench, A., Mckerrow, W.S., Torsvik, T.H., Li, Z.X., McCracken, S.R., 1993. The polarity of the Silurian magnetic field: indications from a global data compilation. *J. Geol. Soc.* 150, 823–831.
- Tucker, R.D., Bradley, D.C., Ver Straeten, C.A., Harris, A.G., Ebert, J.R., McCutcheon, S.R., 1998. New U–Pb zircon ages and the duration and division of Devonian time. *Earth Planet. Sci. Lett.* 158, 175–186.
- van der Meer, D.G., Spakman, W., van Hinsbergen, D.J.J., Amaru, M.L., Torsvik, T.H., 2010. Towards absolute plate motions constrained by lower-mantle slab remnants. *Nat. Geosci.* 3, 36–40.
- van der Meer, D.G., Zeebe, R.E., van Hinsbergen, D.J., Sluijs, A., Spakman, W., Torsvik, T.H., 2014. Plate tectonic controls on atmospheric CO₂ levels since the Triassic. *Proc. Natl. Acad. Sci.* 111, 4380–4385.
- van der Meer, D.G., van den Berg van Saparoea, A.P.H., van Hinsbergen, D.J.J., van de Weg, R.M.B., Godderis, Y., Le Hir, G., Donnadieu, Y., 2017. Reconstructing first-order changes in sea level during the Phanerozoic and Neoproterozoic using strontium isotopes. *Gondwana Res.* 44, 22–34.
- van der Meer, D.G., van Hinsbergen, D.J.J., Spakman, W., 2018. Atlas of the Underworld: slab remnants in the mantle, their sinking history, and a new outlook on lower mantle viscosity. *Tectonophysics* 723, 309–448.
- Vêrard, C., Hochard, C., Baumgartner, P.O., Stampfli, G.M., Liu, M., 2015. Geodynamic evolution of the Earth over the Phanerozoic: plate tectonic activity and palaeoclimatic indicators. *J. Palaeogeogr.* 4, 167–188.
- Voice, P.J., Kowalewski, M., Eriksson, K.A., 2011. Quantifying the timing and rate of crustal evolution: global compilation of radiometrically dated detrital zircon grains source. *J. Geol.* 119, 109–126.
- Wada, I., King, S., 2015. Dynamics of Subducting slabs: numerical modeling and constraints from seismology, geoid, topography, geochemistry, and petrology. In: Bercowski, D. (Ed.), *Mantle Dynamics*, second ed. Elsevier, Amsterdam, pp. 339–391.
- Wicht, J., Stellmach, S., Harder, H., 2010. Numerical dynamo simulations: from basic concepts to realistic models. In: Freedman, W., Nashed, M.Z., Sonar, T. (Eds.), *Handbook of Geomathematics*. Springer, Berlin.
- Yang, Z., Otofujii, Y., Sun, Z., Huang, B., 2002. Magnetostratigraphic constraints on the Gondwanan origin of North China: Cambrian/Ordovician boundary results. *Geophys. J. Int.* 151, 1–10.
- Zhang, N., Zhong, S.J., 2011. Heat fluxes at the Earth's surface and core-mantle boundary since Pangea formation and their implications for the geomagnetic superchrons. *Earth Planet. Sci. Lett.* 306, 205–216.